DISCRETE SNAKING: MULTIPLE CAVITY SOLITONS IN SATURABLE MEDIA*

A.V. YULIN † AND A.R. CHAMPNEYS ‡

Abstract. A one-dimensional lattice equation is studied that models the light field in an optical system comprised of a periodic array of optical cavities pumped by a coherent light source. The model includes effects of linear detuning, linear and nonlinear dissipation and saturable nonlinearity. A wide variety of different parameter regions are studied in which there is bistability between low-power and high-power spatially homogeneous steady states. By posing the steady problem as a time-reversible four-dimensional discrete map, it is shown that temporal stability of these states is a necessary condition for the existence of spatially localised modes. Numerical path-following is used to find both so-called bright solitons (whose core is at higher intensity than the tails) and grey solitons (with non-zero lower intensity tails), whose temporal stability is also computed.

Starting from the case of focusing nonlinearity in the continuum limit and with energy conservation, the effects of dissipation and spatial discreteness are studied both separately and in combination. The presence of Maxwell points, where heteroclinic connections exist between different homogeneous states is found to lead to snaking bifurcation diagrams where the width of the soliton grows via a process of successive increase and decrease of a parameter representing the pump strength. These structures are found to cause parameter intervals where there are infinitely many distinct stable solitons, both bright and grey. Mechanisms are revealed by which the snakes can be created and destroyed as a second parameter is varied. In particular, the bright solitons reach the boundary of the bistability region where the homogeneous state in the soliton's tail undergoes a fold, whereupon the snake splits into many separate loops. More complex mechanisms underlie the morphogenesis of the grey soliton branches, for example due to a fold of the homogeneous state that forms the core of the snaking soliton.

Further snaking diagrams are found for both defocusing and purely dissipative nonlinearities and yet further mechanisms are unravelled by which the snakes are created or destroyed as a two parameters vary.

Key words. Discrete solitons, Maxwell point, homoclinic snaking, optical cavity, lattice equation

AMS subject classifications. 35Q51, 37L60, 34C15

1. Introduction.

There has been a lot of recent attention on the multiplicity of localised patterns that are organised in so-called homoclinic snaking bifurcation diagrams, see e.g. [2, 4, 3, 12, 23, 16, 20]. The key idea is that an infinite multiplicity of localised structures can coexist in the Pomeau pinning region [26] around a Maxwell point, which is a parameter value at which heteroclinic connections (stationary fronts) can occur between stable patterned and homogeneous background states. In one spatial dimension, the snaking structure can be explained by the presence of beyond-all-orders terms in a weakly nonlinear (normal form) description of these Pomeau fronts [20]. These terms lead to heteroclinic tangles that cause the creation of infinitely many distinct homoclinic connections (localised patterns) of arbitrarily wide extent [30, 11]. In many contexts, such as that of Swift-Hohenberg theory, each second winding of the snake is temporally stable [2, 3], hence there is an infinite multiplicity of stable structures.

*This work was supported by a research grant from the UK Engineering and Physical Sciences Research Council

†Department of Engineering Mathematics, University of Bristol, Bristol, BS8 1TR, United Kingdom (a.v.yulin@bristol.ac.uk).

‡Department of Engineering Mathematics, University of Bristol, Bristol, BS8 1TR, United Kingdom

Recently, the present authors [32] announced the presence of homoclinic snaking and the corresponding infinite multistability of stationary patterns in a spatially discrete model for an optical cavity with an imposed periodic structure and saturable nonlinearity. The model can be written in dimensionless form as the one-dimensional lattice equation for a complex field $A_n \in \mathbb{C}$, $n \in \mathbb{Z}$:

$$i\partial_t A_n + \delta A_n + \frac{\alpha|A_n|^2}{1+|A_n|^2}A_n + c(A_{n+1} + A_{n-1} - 2A_n) = P. \tag{1.1}$$

The study of such a model system generalises the earlier work of Egorov *et al.* [24, 14, 15] who considered a similar lattice model with pure cubic nonlinearity and a model with two components coupled by so-called $\chi^{(2)}$ quadratic nonlinearity. The variable A_n represents the amplitude of the field inside the n-th identical optical resonator in a one-dimensional array; see Fig. 1.1. Stationary localised patterns in such physical devices are of interest due to their potential use in optical information processing systems [25]. We shall henceforth refer to such localised states as "solitons", as is common in the physics literature, even though our model is non-integrable.

The parameters appearing in (1.1) can be explained as follows. The coefficient $c \geq 0$ represents the strength of the nearest-neighbour coupling between oscillators due to their evanescent field. The limit $c \to \infty$ corresponds to the continuum limit, whereas $c \to 0$ represents the so-called anti-continuum limit in which the oscillators are independent of each other. The parameter P measures the amplitude of an applied optical pump field which for simplicity we suppose to be real and independent of n, which would correspond to a spatially homogeneous pump wave with normal incidence. The real part of δ represents detuning of the pump frequency from the resonant frequency of the oscillators. The parameter α represents the strength of the Kerr effect of intensity-dependent refractive index, where the physically realistic effect of saturation for large intensity has been included. The field strength has been scaled so that the saturation constant (the coefficient multiplying $|A|^2$ in the denominator of the nonlinear term of (1.1)) has been set to unity. Let us note here that such saturable nonlinearity can be found in a variety of different optical systems, for example in semiconductors, where their would also be the presence of loss due to photon absorption [31]. In general, δ and α can be complex; their imaginary parts represent linear and nonlinear loss terms respectively. In this work we consider only passive media which implies that the imaginary part of the effective detuning $\mathrm{Im}(\delta + \frac{\alpha|A|^2}{1+|A|^2})$ must be positive for all A. Thus, we must have

$$\mathrm{Im}(\delta) \geq 0 \quad \text{and} \quad \mathrm{Im}(\delta + \alpha) \geq 0. \tag{1.2}$$

In an earlier paper [32] we announced the presence of many bright discrete solitons (localised states with the intensity of the central core above that of the background state) and grey solitons (with core intensity below that of the background state) for the particular parameter region $-9\alpha/8 < \delta < -\alpha < 0$. These results will be expanded upon in Sec. 3.4 below. The solitons lie on snaking curves in a bifurcation diagram as P varies, leading to parameter intervals in which there are infinitely many *stable* solitons. Egorov *et al* [24, 15] had earlier found discrete localised structures in a similar model with different nonlinearity that exhibits neither bistability nor localised structures for the case considered in [32]. Our previous paper also explained why snaking bifurcation diagrams of this nature should occur in general classes of discrete optical systems like (1.1), by appealing to the same generic argument for discrete

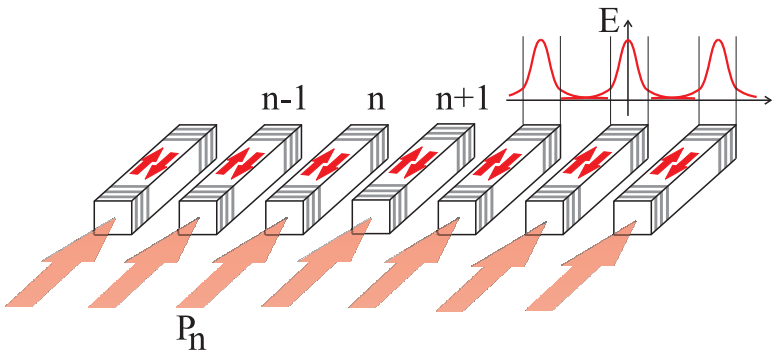

FIG. 1.1. *Sketch of a periodic optical structure composed of identical resonators pumped by coherent light such as would be described by a model of the form (1.1). The electric field concentrated inside the nth optical resonator can be characterised by a complex amplitude A_n, and P_n represents the corresponding pump field. The evanescent fields (labelled E) outside the resonators are responsible for the coupling between each A_n. In this work P_n is assumed to be a constant P independent of n, and without loss of generality the origin of phase is chosen so that P is real.*

dynamical systems as those that were applied in [30, 11, 2] for Poincaré maps of continuous systems.

The purpose of the present paper then is to provide a comprehensive study of stationary localised solutions to (1.1), providing many more details of the homoclinic snaking mechanisms than in [32], and also dealing with a much wider selection of values of the various parameters. In particular, we shall additionally treat both defocusing ($\mathrm{Re}(\alpha) < 0$) and purely dissipative ($\mathrm{Re}(\alpha) = 0$) nonlinearities, as well the full range of parameters for focusing nonlinearity ($\mathrm{Re}(\alpha) > 0$) for which there is multiplicity of homogeneous states. A particular focus will be to reveal many qualitatively distinct snaking curves as P-varies, depending on the values of the other parameters, and to uncover the mechanisms by which these snakes are created or destroyed as a second parameter is varied. In so doing we shall also pay attention to the temporal stability of all the stationary patterns that we find. A brief qualitative summary of our results is contained in Table 1.1

The rest of the paper is outlined as follows. Section 2 provides a comprehensive examination of homogeneous solutions to (1.1), highlighting in particular those parameter regions where such states have the correct linearisation to support localised solutions. By recasting the steady equations as a spatial dynamical system, we show the correspondence between hyperbolicity and temporal stability, both of which are necessary to see stable solitons. Sections 3–5 contain the main results from numerical path following and stability analysis of soliton solutions. We start from the simplest case of a pure conservative system $\mathrm{Im}(\delta) = \mathrm{Im}(\alpha) = 0$ for focusing nonlinearity $\alpha > 0$ in the continuum limit $c \to \infty$ and slowly build up complexity of the bifurcation diagrams by moving to different parameter regimes. While the results are reasonably comprehensive, they are presented in a pedagogical order to successively highlight new features rather than to exhaustively explore parameter space. Thus, most space is dedicated to the treatment of focusing nonlinearity (Sec. 3), and rather less to defocusing (Sec. 4) and pure dissipative (Sec. 5) nonlinearities. Finally, Sec. 6 draws conclusions, by highlighting the new codimension-two processes that have been presented for the birth and destruction of snaking bifurcation diagrams and points to methods of analysis that might explain these results.

Parameters				Sec.	Figs.	Description
α	c	$\mathrm{Re}(\delta)$	$\mathrm{Im}(\delta)$			
>0	$\to\infty$	$-\alpha<\delta<0$	0	3.1	2.2(a), 3.1, 3.2	bright solitons & multi-pulses
>0	$\to\infty$	$-\alpha<\mathrm{Re}(\delta)<0$	>0	3.2	2.2(c), 3.3 – 3.7	thin snakes of bright and grey solitons for large enough $\mathrm{Im}(\delta)$
>0	finite	$-\alpha<\mathrm{Re}(\delta)<0$	>0	3.3	2.2(b),3.8–3.12	wide snakes of bright and grey solitons
>0	finite or $\to\infty$	$-\frac{9\alpha}{8}<\mathrm{Re}(\delta)<-\alpha$	≥ 0	3.4	2.3, 3.13–3.16	snakes of bright and grey solitons
<0	$\to\infty$	$0<\mathrm{Re}(\delta)<\frac{9\alpha}{8}$	0	4.1	2.4(a,b),2.5(a),4.2– 4.1	topological solitons
<0	finite or $\to\infty$	$0<\mathrm{Re}(\delta)<\frac{9\alpha}{8}$	>0	4.2	2.4(c),2.5(b),4.3–4.7	wide snakes of bright and grey snakes
imag.	$\to\infty$	$\mathrm{Re}(\delta)<0$	>0	5	2.6,5.1–5.3	wide and thin snakes of bright and grey snakes

TABLE 1.1

Qualitative description of kinds of snaking bifurcation curves found for (1.1). The limit $c\to\infty$ represents the continuum limit, whereas finite c corresponds to a discrete lattice.

2. Homogeneous states. Let us begin by considering the simplest steady states of the problem, homogeneous states $A_n(t)=A$ which satisfy

$$\left(\delta+\frac{\alpha|A|^2}{1+|A|^2}\right)A=P. \tag{2.1}$$

For fixed P, Eq. (2.1) can have either one or three solutions and our first task is to characterise when each case occurs. We shall consider separately focusing ($\alpha>0$), defocusing ($\alpha<0$) and dissipative ($\mathrm{Re}(\alpha)=0$) nonlinearities. Since our goal is ultimately to study physically realisable stationary solitons, we also need to study the stability problem because experimentally observable solitons cannot reside on an unstable background.

To determine the stability of a homogeneous state A, we need to consider the linearised equation for a small correction $a_n(t)$ to the homogeneous field $A_n=A+a_n(t)$:

$$i\partial_t a_n+\left(\delta+\alpha\frac{2|A|^2+|A|^4}{(1+|A|^2)^2}\right)a_n+\frac{\alpha(A)^2}{(1+|A|^2)^2}a_n^*+ \\ +c(a_{n+1}+a_{n-1}-2a_n)=0, \tag{2.2}$$

where an asterisk denotes complex conjugation. Solutions can be sought in the form $a_n = e^{\lambda t}e^{iqn}$, where q is the spatial frequency of an eigenmode. First, note that for boundedness as $n \to \pm\infty$, q must be real. Without loss of generality we can assume $q \in [0, \pi]$. Then, after some algebra we find

$$\lambda(q) = -\mathrm{Im}(\delta + \alpha + r) \pm \sqrt{|p|^2 - [\mathrm{Re}(\alpha + \delta + r) + 2c(\cos(q) - 1))]^2}, \tag{2.3}$$

where $r = -\frac{\alpha}{(1+|A|^2)^2}$ and $p = rA^2$. For stability we require that $\mathrm{Re}[\lambda(q)] \leq 0$, for all $q \in [0, \pi]$. Hence, from (2.3) and the fact that $\mathrm{Im}(\Delta) > 0$ by assumption (1.2), we require

$$\max_{q\in[0,\pi]} \left\{|p|^2 - [\mathrm{Re}(\Delta) + 2c(\cos(q) - 1)]^2\right\} \leq [\mathrm{Im}(\Delta)]^2, \tag{2.4}$$

where $\Delta = \alpha + \delta + r$. Instability upon varying a parameter occurs when we reach a point where $\max_{q\in[0,\pi]}\lambda = 0$, which implies equality in (2.4). We can identify three possible forms of codimension-one instability as follows.

Fold: this is the only generic form of spatially homogeneous instability and occurs when the maximum in (2.4) is achieved for $q = 0$. From (2.4) we see that $\mathrm{Re}(\Delta) \leq 0$ at such a point, and we have

$$[\mathrm{Im}(\Delta)]^2 = |p|^2 - [\mathrm{Re}(\Delta)]^2. \tag{2.5}$$

Spatially alternating modulation instability: this occurs when $\mathrm{Re}(\Delta) \geq 4c$ so that the maximum is achieved in the second equation (2.4) when $q = \pi$. The condition for this instability is thus

$$[\mathrm{Im}(\Delta)]^2 = |p|^2 - [\mathrm{Re}(\Delta) - 4c]^2. \tag{2.6}$$

General modulation instability: this form of instability occurs when $0 < \mathrm{Re}(\Delta) < 4c$ so that the maximum is achieved when $\cos(q) = 1 - (1/2c)\mathrm{Re}(\Delta)$. This gives the condition for this instability to occur to be precisely when

$$\mathrm{Im}(\Delta) = |p|. \tag{2.7}$$

Note that in the conservative case, this kind of instability cannot occur other than for the equilibrium $A = 0$, because $\mathrm{Im}(\Delta) = 0$.

Another necessary condition for the presence of stable solitons is that we have the possibility of decay in space to a homogeneous state as $n \to \pm\infty$. To find a condition for this, it is helpful to view the equilibrium equation for stationary solutions of (1.1) as a *spatial dynamical system* in the discrete "evolution" variable $n \in Z$:

$$A_{n+1} = A_n + B_n + \frac{1}{c}\left(P - \delta A_n - \frac{\alpha|A_n|^2}{1 + |A_n|^2}A_n\right) \tag{2.8}$$

$$B_{n+1} = B_n + \frac{1}{c}\left(P - \delta A_n - \frac{\alpha|A_n|^2}{1 + |A_n|^2}A_n\right). \tag{2.9}$$

Thus, the system (2.8), (2.9) is a 2D reversible map for (A_n, B_n) in $\mathbb{C}^2$, where the additional variable $B_n = A_n - A_{n-1}$ measures the slope of the soliton at a point between lattice sites n and $n - 1$. See e.g. [22] for the general properties of reversible maps. Specifically, reversibility in this context means that the system is invariant under the transformations

$$R_1 : (A_n, B_n) \leftrightarrow (A_{-n}, -B_{1-n}),$$

$$R_2 : (A_n, B_n) \leftrightarrow (A_{1-n}, -B_n),$$

and reversal of the direction of iteration. The fixed-point sets of these transformations give boundary conditions for solutions with different kinds of symmetry

$$\text{on-site centred: } A_{-1} = A_1, \quad B_0 = -B_1, \tag{2.10}$$

$$\text{off-site centred: } A_{-1} = A_0, \quad B_0 = 0. \tag{2.11}$$

Note that any spatially homogeneous solution corresponds to a fixed point of (2.8), (2.9) with $B_n = 0$, which is necessarily symmetric with respect to both R_1 and R_2. To find the possibility of localised states that relax exponentially to such a fixed point as $n \to +\infty$, we require that the map linearised about the fixed point has a Floquet multipliers inside the unit circle. Similarly, to be able to exponentially relax to the fixed point as $n \to -\infty$ there must be a multiplier outside the unit circle. By standard results [22], spatial reversibility ensures that for every multiplier μ there must be a multiplier $1/\mu$ and hence the presence of an expanding multiplier $|\mu| > 1$ ensures the presence of a decaying multiplier $|\mu| < 1$. Now, for any such localised state to be persistent as parameters vary (in the absence of integrability or any additional invariant subspaces) the dimensions of the stable and unstable manifolds of the fixed point must sum to the dimension of the system. Hence in order to find branches of localises states as a single parameter varies, we require that the fixed point must be *hyperbolic*, i.e. have no multipliers on the unit circle.

To find the Floquet multipliers, linearise the time-independent form of (1.1) about some given homogeneous state A. Setting $A(t) = A + a_n$, we obtain

$$\left(\delta + \alpha\frac{2|A|^2 + |A|^4}{\left(1+|A|^2\right)^2}\right) a_n + \frac{\alpha A^2}{\left(1+|A|^2\right)^2} a_n^* + c(a_{n+1} + a_{n-1} - 2a_n) = 0. \tag{2.12}$$

We look for the, in general complex, Floquet multipliers μ by seeking solutions of Eq. (2.12) in the form $a_{n+1} = \mu a_n$. This implies μ must satisfy quadratic equation

$$\mu^2 + 2(\xi - 1)\mu + 1 = 0, \tag{2.13}$$

where

$$\xi = \frac{1}{2c}\left(\mathrm{Re}\,(\alpha + \delta + r) \pm \sqrt{|p|^2 - \left(\mathrm{Im}(\alpha + \delta + r)\right)^2}\right), \tag{2.14}$$

and $r(A)$ and $p(A)$ were defined earlier. Hence, a sufficient condition for all multipliers μ to not lie on the unit circle is

$$|\xi - 1| > 1, \tag{2.15}$$

for both branches of ξ given by (2.14). Let us now analyse possible bifurcation points at which hyperbolicity given by (2.15) can be lost.

Consider first the case where ξ is real. There are two ways in which $|\xi - 1| = 1$, namely $\xi = 0$ or $\xi = 2$. In the former case, we have $\mathrm{Re}(\Delta) + \sqrt{|p^2| - [\mathrm{Im}(\Delta)]^2} = 0$, where $\Delta = \alpha + \delta + r$ as above, and we choose the sign '+' because we must have $\mathrm{Re}(\Delta) < 0$ in order to have all other multipliers off the circle in this case. Hence we obtain $[\mathrm{Im}(\Delta)]^2 = |p|^2 - [\mathrm{Re}(\Delta)]^2$, which is precisely the condition (2.5) for a fold in the temporal dynamics. Alternatively, if $\xi = 2$, we have $\mathrm{Re}(\Delta) - \sqrt{|p|^2 - [\mathrm{Im}(\Delta)]^2} = 4c$,

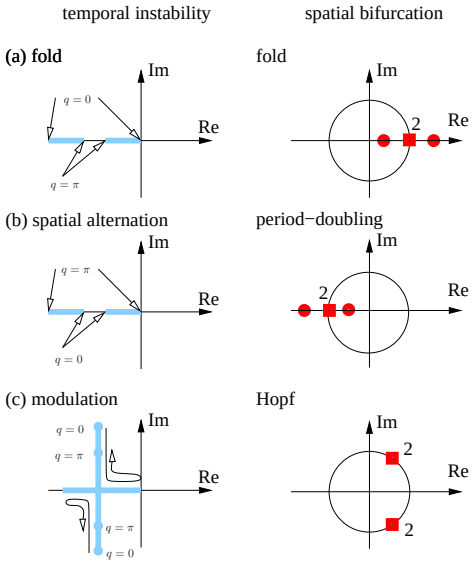

FIG. 2.1. *The correspondence between temporal instability and loss of hyperbolicity for the spatial dynamics problem. The left-hand plot in each case represents the eigenvalues $\lambda(q)$ given by (2.3). The right-hand plot shows the corresponding Floquet multipliers q that solve (2.13).*

where we choose the sign '$-$' in order to have the other multipliers off the unit circle in this case. Hence we obtain, $[\mathrm{Im}(\Delta)]^2 = |p|^2 - [\mathrm{Re}(\Delta) - 4c]^2$, which was precisely the condition (2.6) for a modulation instability with spatial frequency π, which we identify here as a spatial period-doubling bifurcation.

Finally, consider the case when ξ is complex. Then the multipliers form a complex quadruple: μ_1, $\mu_2 = 1/\mu_1$, $\mu_3 = \mu_1^*$ and $\mu_4 = 1/\mu_1^*$. The case of interest is when there exists a double eigenvalue so that $\mu_1 = \mu_2$, which would generically imply a spatially reversible Hopf (torus) bifurcation of the map (see Fig 2.1). Then, since

$$\mu_1^2 + \frac{1}{2c}\left(\mathrm{Re}(\Delta) - 2c + \sqrt{|p^2| - [\mathrm{Im}(\Delta)]^2}\right)\mu_1 + 1 = 0$$

$$\text{and} \quad \mu_2^2 + \frac{1}{2c}\left(\mathrm{Re}(\Delta) - 2c - \sqrt{|p^2| - [\mathrm{Im}(\Delta)]^2}\right)\mu_2 + 1 = 0,$$

upon setting $\mu_1 = \mu_2$ and subtracting, we find $\sqrt{|p^2| - [\mathrm{Im}(\Delta)]^2} = 0$, which only leads to eigenvalues on the unit circle if $0 < \mathrm{Re}(\Delta) < 4c$. But these were precisely the conditions for a general (non-spatially alternating) temporal modulation instability.

Hence, we have established the correspondence between temporal instabilities and local bifurcations of the corresponding reversible fixed point summarised in Fig. 2.1. These arguments can easily be extended to establish the following:

PROPOSITION 2.1. *If the spatially homogeneous equilibrium $A_n(t) = A$ of (1.1) is stable then the corresponding fixed point $A_n = A$ of the reversible map is hyperbolic. Conversely, if the fixed point of the map is hyperbolic then there are either zero or two unstable branches of linear spectrum of the temporal problem linearised about the homogeneous equilibrium.*

With these general results in hand, we can analyse the existence and stability of homogeneous solutions in various parameter regimes of interest.

2.1. Focusing nonlinearity, $\alpha > 0$. In the conservative case $\mathrm{Im}(\delta) = 0$ it is possible to distinguish an interval of the linear detuning δ where multiple homogeneous states occur. Specifically, if $-\alpha < \delta < 0$ then the linear detuning can be compensated by the nonlinear correction. Thus, at zero pump $P = 0$, there are two equilibrium states, the trivial one and a solution with intensity $|A|^2 = \frac{-\delta}{\alpha+\delta}$ and arbitrary phase. The phase symmetry is broken by the introduction of non-zero pump and the high-intensity state splits into two. At the same time, the trivial state becomes nonzero. This multiplicity of solution with upper, intermediate and lower intensity persists until the lower and intermediate states merge and annihilate each other in a fold bifurcation at pump value

$$P_+ = A_+\left(\delta + \frac{\alpha|A_+|^2}{1+|A_+|^2}\right), \quad \text{where} \quad A_+ = \sqrt{\frac{-3\alpha - 2\delta + \sqrt{9\alpha^2 + 8\alpha\delta}}{2(\alpha+\delta)}}\,.$$

The dependence of the absolute value of the field A on P is shown in the upper part of Fig. 2.2 (for the sake of convenience the vertical and horizontal axis are swapped from the usual convention for bifurcation diagrams).

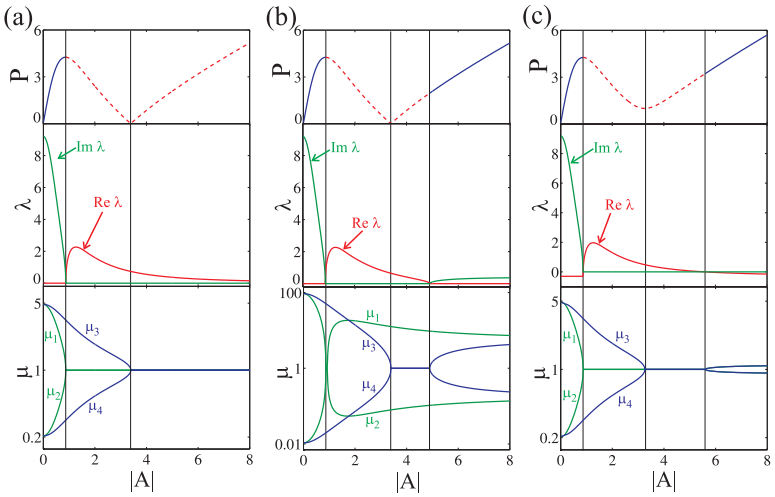

FIG. 2.2. *Bifurcation diagram of homogeneous steady states $A_n(t) = A$ to (1.1) for $\alpha = 10$ and $Re(\delta) = -9.2$. The other parameters used are (a) $c = 3$, $Im(\delta) = 0$ (conservative case with strong coupling), (b) $c = 0.1$, $Im(\delta) = 0$ (conservative case with weak coupling), and (c) $c = 3$, $Im(\delta) = 0.3$. The upper panels show the dependence $|A|$ (horizontal axis) against pump P (vertical axis), where solid blue lines represent stable solutions and dashed red lines unstable solutions. The middle panels show the dependence of the real (red lines) and imaginary (green lines) parts of the temporal eigenvalues that have maximal real part. The lowest panels show the absolute value of the spatial Floquet multipliers $|\mu|$.*

From the conditions for linear stability (2.4) it is possible to conclude that the lower branch is always stable and the intermediate branch is always unstable. For sufficiently strong coupling, $4c > \delta + \alpha$, the upper branch is always unstable; see the middle plot Fig. 2.2(a) which shows the real and imaginary parts of the maximum real-part temporal eigenvalues. For weak coupling $4c < \delta + \alpha$, the upper branch restabilises at sufficiently high pump-values, due to a reverse spatially-alternating modulation instability.

The introduction of loss, $\mathrm{Im}(\delta) \neq 0$, makes it impossible for the non-trivial solution to exist at zero pump, and so the high-intensity branch shifts from the horizontal

axis in the upper panel of Fig. 2.2(c) and the multiplicity region shrinks. If the loss becomes too big then the multiplicity ceases to occur at all.

The bottom row of plots in Fig. 2.2 depicts the behaviour of the absolute value of the Floquet multipliers along the branches of homogeneous states. There are four separate curves in general. Two curves being overlaid along the line $|\mu| = 1$ correspond to a pair of multipliers on the unit circle. Where only one curve is apparent, then all four Floquet multipliers are on the unit circle. For weak coupling, at the pump value where the upper branch stabilises, we see a spatially-alternating modulation instability. Hence if solitons exist that decay to the equilibrium on the upper curve, they must have oscillatory tails.

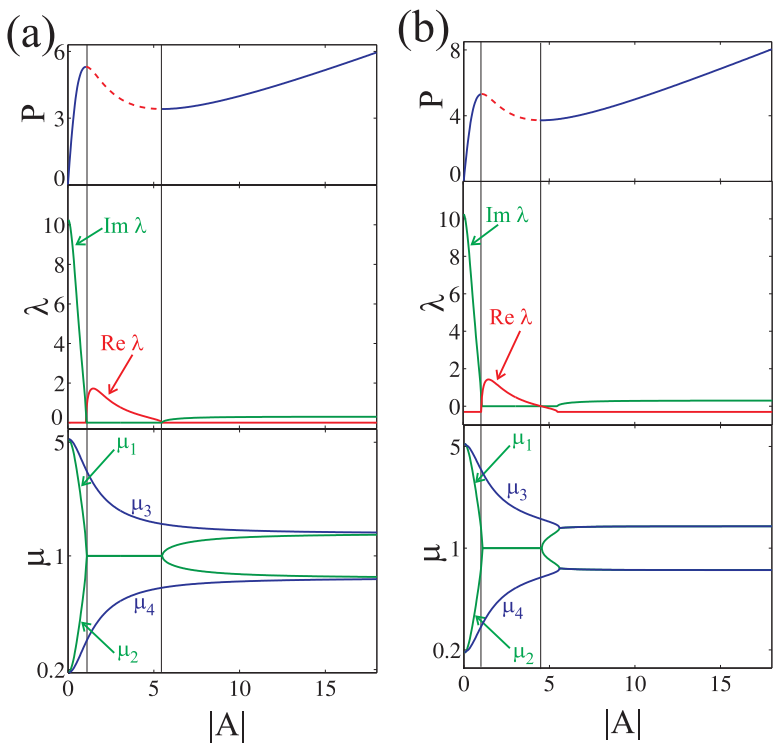

FIG. 2.3. *Similar to Fig. 2.2, but for* $\delta = -10.3$ *in (a) and* $\delta = -10.3 + 0.3i$ *in panel (b). The coupling strength is* $c = 3$ *in both cases.*

If the linear detuning is real and negative but too big $-\delta > \alpha$ then it cannot be compensated by the nonlinear correction to the detuning. Thus, at zero pump the system can have only the trivial homogeneous solution. But multiplicity survives provided detuning is in the range $-9\alpha/8 < \delta < -\alpha$, specifically when $P \in [P_-, P_+]$, given by

$$P_\pm = A_\pm \left(\delta + \frac{\alpha |A_\pm|^2}{1 + |A_\pm|^2} \right), \qquad \text{where } A_\pm = \sqrt{\frac{-3\alpha - 2\delta \pm \sqrt{9\alpha^2 + 8\alpha\delta}}{2(\alpha + \delta)}}.$$

This kind of multiplicity cannot take place in the case of pure cubic nonlinearity. The bifurcation diagram for this case is shown in the upper part of Fig. 2.3(a). Note that the introduction of a small loss term $\mathrm{Im}(\delta) > 0$ does not qualitatively change the shape

of the solution branches, see Fig. 2.3(b) — although the width of multiplicity region shrinks. If the loss becomes too strong though, the multiplicity region disappears altogether.

The lower two rows of panels of Fig. 2.3 provide information on the stability of the homogeneous states for this range of moderate detuning $-9\alpha/8 < \mathrm{Re}(\delta) < -\alpha$. In this case, both the lower and upper branches are always stable. Thus, in this parameter regime there may be solitons with tails that relax to either of the lower or the upper homogeneous state. The Floquet multipliers show that the spatial decay to the lower state is always monotonic, whereas for $\mathrm{Im}(\delta) > 0$, homoclinic connections to the upper state generally have decaying oscillatory tales.

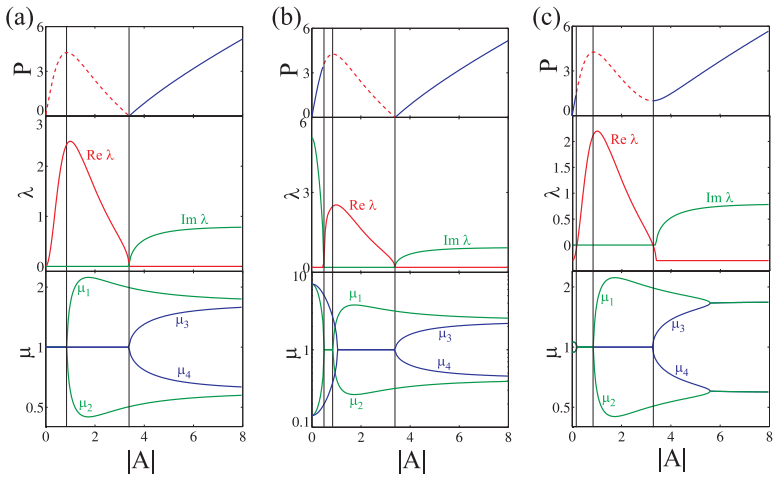

FIG. 2.4. *Similar to Fig. 2.2, but for the defocusing nonlinearity* $\alpha = -10$ *and* $Re(\delta) = 9.2$. *Parameter values used are (a)* $c = 3$, $Im(\delta) = 0$ *(conservative case with strong coupling), (b)* $c = 1$, $Im(\delta) = 0$ *(conservative case with weaker coupling), and (c)* $c = 3$, $Im(\delta) = 0.3$ *(dissipative case with strong coupling).*

2.2. Defocusing nonlinearity, $\alpha < 0$**.** Note that the equation (2.1) for the amplitude of the homogeneous state is symmetric with respect to the change

$$\alpha \to -\alpha, \qquad \delta \to -\delta \tag{2.16}$$

Thus, for the lossless case $\mathrm{Im}(\delta) = 0$, analogous results to the case with $\alpha > 0$ exist if we change the sign of δ, see Fig. 2.4. However, the equation (2.2) governing stability of homogeneous states is not symmetric with respect to (2.16). So, whereas the bifurcation curves look exactly the same as in the case of focusing nonlinearity, their stability properties are different. An example of the case $0 < \delta < -\alpha$ is shown in Fig. 2.4, from which we see that the upper homogeneous state is stable in all cases and the intermediate state always unstable. The lower branch is also unstable in the conservative case with strong coupling. For sufficiently weak coupling, specifically $4c < \delta$, part of lower branch becomes stable between a $P = 0$ and a lower-P threshold representing a modulation instability. Introduction of linear loss can similarly partly stabilise the lower branch. Thus, whereas the upper branch is always capable of supporting solitons, the lower branch can only do so in the case of weak coupling or in the presence of loss.

If the linear detuning is in the intermediate interval $-\alpha < \mathrm{Re}(\delta) < -9\alpha/8$ then all branches are unstable in the conservative case and for strong coupling. In the

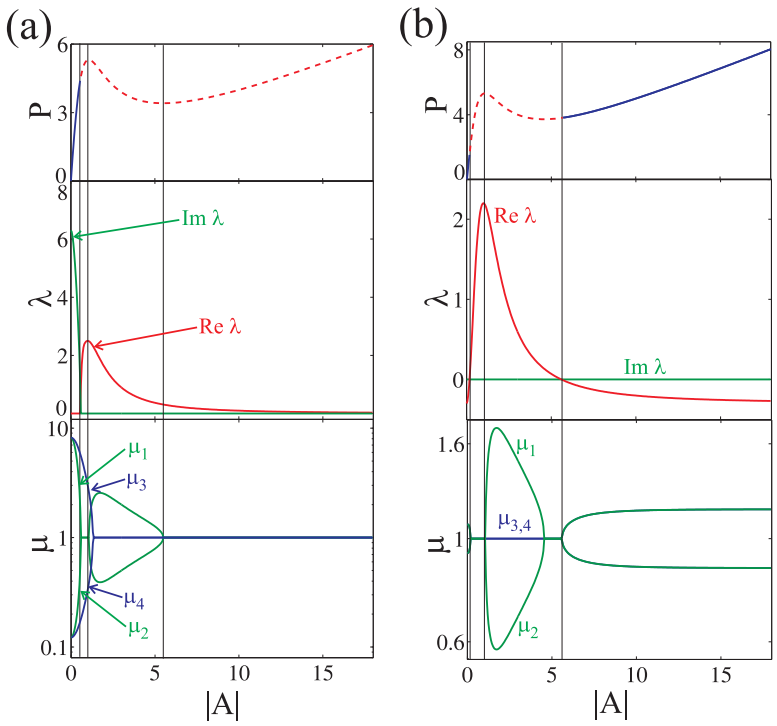

FIG. 2.5. *Similar to Fig. 2.3, but for the defocusing case* $\alpha = -10$. *Other parameters are (a)* $\delta = 10.3$, $c = 3$; *and (b)* $\delta = 10.3 + 0.3i$, $c = 1$.

case of weak coupling though, part of the lower branch is stable, see the middle panel of Fig. 2.5(a). In the presence of linear loss, Fig. 2.5(b) shows that both the lower and upper branches can be partly stable. One can see that there may be spatially alternating relaxation to the lower state (corresponding to real negative Floquet multipliers) for sufficiently weak coupling. In the case with loss the relaxation is always oscillatory (corresponding to complex multipliers).

2.3. Pure dissipative nonlinearity, Re(α) = 0. The last case we shall consider is that of pure dissipative nonlinearity. It is easy to notice that the change $\alpha \to i\alpha$, $\delta \to i\delta$, $A \to -iA$ does not alter Eqn. (2.1). Hence many of the conclusions reached from the case of conservative nonlinearity still apply. A subtle distinction though is that the real part of δ now plays the role that Im(δ) played in the case of conservative nonlinearity, and vice versa. Also the homogeneous states are $\pi/2$ out of phase with the pump.

In the pure dissipative case where Re(δ) = 0, multiplicity of homogeneous states occurs for parameters in the interval

$$0 < -\mathrm{Im}(\alpha) < \mathrm{Im}(\delta) < -\frac{9}{8}\mathrm{Im}(\alpha).$$

Introduction of real linear detuning decreases the multiplicity region until, at a critical detuning value, it disappears altogether. The bifurcation curves are shown in the upper part of Fig. 2.6. Note that the sign of the linear detuning does not affect the existence of homogeneous states, but it does affect their stability. The intermediate branch is always unstable. If the detuning is positive, Re(δ) > 0, then the parts of

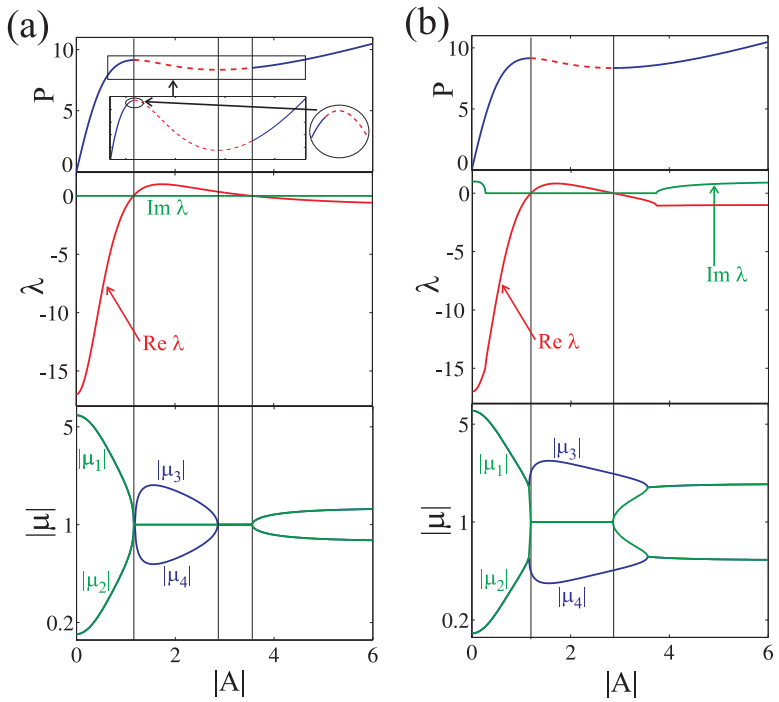

FIG. 2.6. *Similar to Fig. 2.2, but for the dissipative nonlinearity* $\alpha = -16i$. *The linear detuning is* $\delta = 1 + 17i$ *for case (a) and* $\delta = -1 + 17i$ *for (b). The coupling strength is* $c = 3$. *The inserts in the upper part the bifurcation diagram in (a) show the multiplicity region in more detail.*

the lower and upper branches in the vicinity of the the folding points are unstable; see Fig. 2.6(a) — whereas for $\mathrm{Re}(\delta) < 0$ both the lower and the upper branches are completely stable. The corresponding Floquet multipliers are shown in the lower panels of Fig. 2.6. One can see that in the case of positive detuning the relaxation to both the lower and upper stable states is oscillatory. In the case of negative detuning though, the spatial relaxation to stable states can be monotonic or oscillatory. Note finally that for dissipative nonlinearity there is no threshold that distinguishes strong and weak coupling; the results are qualitatively the same regardless of the coupling strength.

3. Solitons for focusing nonlinearity. Let us now proceed to consider localised stationary solutions to (1.1) in the parameter regimes where we have identified stable homogeneous states. The method for computing the solitons is via a dedicated path-following code that we have developed in Matlab, which truncates to a large finite interval $n \in [-N, N]$ using periodic boundary conditions and poses the appropriate symmetry condition (2.10) or (2.11) around $N = 0$ to compute either site-centred or off-site-centred solitons. This enables us to compute only on the interval $[0, N]$ and results in N complex algebraic equations that can be solved using Newton's method aligned to pseudo-arclength continuation (see e.g. [21]).

Temporal stability of the solitons can be studied by computing the spectrum of the equations (1.1) linearised around a stationary localised solution A_n, $n = -\infty, \ldots \infty$ (that is, Eqns. (2.2) with A replaced by a A_n). Due to the lattice structure, this spectrum will consist of an infinite set of eigenvalues that are well represented under

truncation to $-N < n < N$, for N sufficiently large. Generally speaking, we expect to see solitons that are either exponentially unstable (with some eigenvalues having positive real part) or are stable. For the dissipative case, we would have asymptotic stability when all eigenvalues have negative real part, whereas in the conservative case the best we can hope for is Lyapunov stability where all eigenvalues are on the imaginary axis. We check for stability, by simply using Matlab to compute the eigenvalues of the truncated linearised problem, which matrix is formed anyway in order to implement the arclength continuation. We also check the mechanism of instability by direct simulation of (1.1) using perturbations of the computed solitons as initial conditions.

We shall present results on a case-by-case basis, starting from the simplest possible assumptions of a conservative system in the continuum limit with weak detuning, and then slowly increase the complexity of the problem.

3.1. Conservative system in the continuum limit with weak detuning. Consider the conservative system $\mathrm{Im}(\delta) = 0$ with weak detuning $-\alpha < \delta < 0$ in the limit of large c, in which case we can consider the term $c(A_{n+1} + A_{n-1} - 2A_n)$ to be a numerical approximation of the second derivative of a spatial co-ordinate $X = n/\sqrt{c}$. The stationary equations then admit an invariant subspace in which A is real. Within this subspace, we look for localised solutions of the real equation

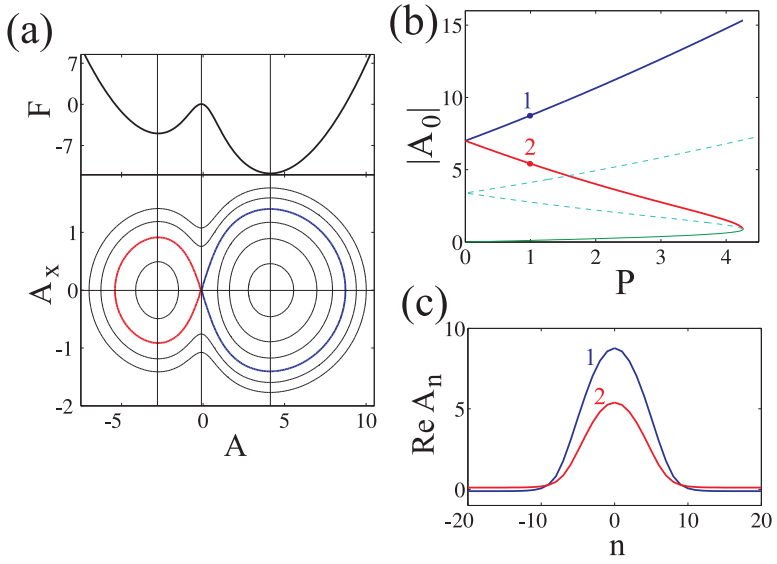

FIG. 3.1. *The potential F and the corresponding phase plane are shown in panel (a) for $\alpha = 10$, $\delta = -9.2$ and $P = 1$. The blue line shows the homoclinic trajectories corresponding to a stable soliton and the red line shows the homoclinic trajectory corresponding to an unstable soliton. The bifurcation diagram showing the dependence of the absolute value of the field in the centre of the soliton as function of the absolute value of the pump is presented in panel (b). The points corresponding to the homoclinic trajectories shown in (a) are marked by "1" and "2". Thinner solid green and dashed cyan lines show the stable and unstable parts of the bifurcation diagram for the homogeneous states. The field distributions in the stable (blue line marked by "1") and unstable (red line marked by "2") solitons are shown in panel (c).*

$$\delta A + \frac{\alpha A^2}{1 + A^2} A + \partial_X^2 A = P, \tag{3.1}$$

which can easily be analysed using phase plane analysis. In particular, letting X play the role of time, (3.1) describes the motion of a particle of unit mass in the potential

$$F = \frac{\delta + \alpha}{2} A^2 - \frac{\alpha}{2} \ln(1 + A^2) - PA. \tag{3.2}$$

For $-\alpha < \delta < 0$, if $P < P_+$, then the potential has three extrema. Each extremum corresponds to a stationary point in the (A, A_X) phase plane; the minima represent centres and the maximum corresponds to a saddle. The shape of the potential and the corresponding phase plane are shown in Fig 3.1(a). At $P = P_+$ one of the minima merges with the maximum and for $P > P_+$ the potential has only one extremum.

The maximum of the potential corresponds to the lower homogeneous solution, whereas the minima correspond to the intermediate and the upper homogeneous solutions. In the case where we have two minima, then there are two homoclinic loops in the phase space, which correspond to solitons of the lattice. Both of these homoclinic loops we shall refer to as *bright solitons* because their maximum $|A|$-value is greater than their asymptotic value as $X \to \pm\infty$. Note, that this consideration of the potential shows one important feature, namely that both branches of solitons exist for the whole region of parameters at which there is multiplicity between the homogeneous states. The low intensity soliton is born in a small amplitude bifurcation at $P = P_+$, the fold point of homogeneous states. This bifurcation is a necessary consequence of the normal form of a fold in a reversible dynamical system, see e.g. [10]. The high-intensity state does not reach zero amplitude at this fold point, but nevertheless must cease to exist there as the background state to which it becomes asymptotic as $X \to \pm\infty$ gets destroyed at the fold. As $P \to P_+$ along this branch, the rate of exponential relaxation in the tail of the soliton decreases, until precisely at $P = P_+$ the decay becomes algebraic rather than exponential. This is a finite-amplitude homoclinic orbit that is contained in the centre manifold of the fold point.

For the parameter values in question, the multiplicity region includes the case $P = 0$. In the absence of the pump, the equations (1.1) admit the S^1 phase symmetry $A \to Ae^{i\phi}$ for any ϕ in $[0, 2\pi)$, and the potential F becomes symmetric under $A \to -A$. So the two real homoclinic loops are mirror images of one another in this case. The presence of non-zero P breaks the phase symmetry and the solitons become distinct, see the bifurcation diagram in Fig 3.1(b).

Each of the family of solitons for (1.1) for $P = 0$ is stable as a solution of the initial value problem, although the spectrum contains four zero eigenvalues that correspond to phase and translation symmetries. When the phase symmetry is broken by introduction of $P > 0$, then for the more intense soliton (labelled "1" in Fig 3.1), a pair of zero eigenvalues become pure imaginary and the soliton remains stable. For the low intensity soliton (labelled "2") the same pair of eigenvalues become pure real and so this soliton branch is unstable.

One might easily imagine that these are the only branches of possible localised states. But the fact that the lower homogeneous branch in Fig. 2.2 has two distinct multipliers outside the unit circle means that the unstable manifold of this state in the continuum spatial dynamics is two-dimensional, moreover solutions in this manifold are not linked by a trivial phase symmetry. Therefore there may be further solitons that asymptote to this background state (generically, any additional states would in fact asymptote to the equilibrium along the *same* spatial eigenvector corresponding to the weakest eigenvalue). In fact, one can also find multi-pulse bright solitons, the bifurcation diagram for which is shown in panel (a) of Fig. 3.2. For the sake of

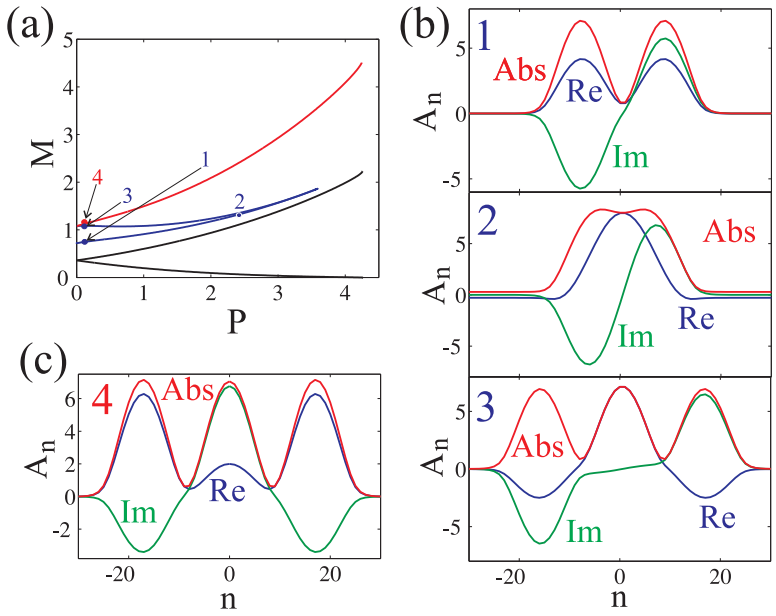

FIG. 3.2. *a) The bifurcation diagram of mass M against pump P for multi-pulse stationary solutions to (1.1) for $\alpha = 10$, $\delta = -9.2$. The coupling constant is $c = 12$ which corresponds effectively to the continuum limit. The black line depicts the single pulses from Fig. 3.1, the blue line shows a branch of of two-pulses that becomes a three pulse, and the red line shows a distinct branch of three-pulses. (b),(c) Field distributions for the labelled points; blue lines show the real parts, green lines show the imaginary parts and the red lines show the absolute values of the fields.*

convenience, solutions in this and subsequent figures are characterised by the norm

$$M = \sum_n (|A_n - A_\infty|^2), \tag{3.3}$$

which describes how much a solitons differs from its background state. We refer to M as being the *mass* of the soliton.

All multi-pulse solitons are complex; see Fig. 3.2(b),(c). The lower branch shown by the black line in panel (a) corresponds to the real-valued single-pulse solitons discussed above. The blue line shows a branch of two-pulse solutions, which as they approach zero pump undergo what has been described as a quasi-nonlocal bifurcation in systems of coupled NLS equations [8]. That is, the branch terminates as P is decreased to zero by the two pulses becoming infinitely widely separated. Hence we see in the bifurcation diagram that the mass of the two-pulse wave becomes twice that of the primary branch. At non-zero pump the interaction between the two far-separated solitons becomes important, which fixes a phase relation between the pulses of the two-pulse branch (see the point labelled "1"). At some higher pump threshold, but still within the bistability region, the bifurcation curve folds back, which causes the appearance of the third pulse in the soliton structure (see the solution graphs at point "3", shown in the lower part of panel (b)).

It is also possible to find another family of three-pulse solitons, represented by the red branch in Fig. 3.2(a); see the graphs in panel (c) of the solution at point "4". It is worth noting that the red curve is not a continuation of the blue curve, which is obvious from their graphs as the two solutions have different symmetry (note in (c)

that the imaginary part is even rather than odd). As this new branch of three-pulses is traced with increasing pump, it reaches the boundary of the multiplicity region, specifically where the homogeneous state that forms the background of this soliton undergoes a fold and ceases to exits. Here, like the high-intensity single-pulse it is destroyed by becoming a finite-amplitude algebraically-decaying soliton.

We conjecture that there are infinitely many m-pulse solution branches, finitely many distinct branches for each number of pulses $m \geq 3$ (corresponding to different symmetry types), which apart from the blue two/three-pulse branch in Fig. 3.2(a) all have the same qualitative features as the red three-pulse branch. That is, they are born in quasi-nonlocal bifurcations at zero pump, and they die at fold point of the lower homogeneous state by becoming becoming algebraically decaying to the background. All the multi-pulse soliton solutions appear to be unstable in the continuum limit. However, as we shall see, the existence of these branches plays a key role in explaining the morphogenesis of more complex bifurcation diagrams when we add dissipation.

3.2. The effect of dissipation. Let us now consider what happens to the above bifurcation diagram if we add linear loss $\mathrm{Im}(\delta) > 0$. As we saw in Fig. 2.2(c), the upper homogeneous state can also become stable for sufficiently high pump, and this stable state can coexist with where the lower state is also stable. Thus we have a genuine bistability region. Bistability opens up the possibility of another kind of localised solution, namely a moving front that connects the two stable homogeneous states. At a specific pump-value known as a Maxwell point [26], these fronts become stationary. Perturbations of the pump from this value will cause fronts to move either to the left or to the right. This definition accords with the more usual definition of Maxwell points in integrable Hamiltonian systems as being where two equilibrium states have equal energy (which is a necessary rather than sufficient condition for a stationary heteroclinic connection is such a case). However, since this paper ultimately concerns dissipative discrete systems, we shall use a wider working definition of a Maxwell point as being the parameter value at which a heteroclinic connection exists between bistable equilibrium states. As we shall see, for fixed points of maps, or equivalently connections between periodic structures in continuum systems, one typically sees not an isolated Maxwell point by a *pinning region* parameter space for which such heteroclinic connections (stationary fronts) exist, see e.g. [26, 30, 11].

Returning to the case at hand, two branches of solitons approach the Maxwell point, a bright soliton (homoclinic orbit to the lower homogeneous state) and a *grey soliton* (homoclinic to the upper homogeneous state). Note that the Floquet multipliers of the upper homogeneous state are complex at the Maxwell point and lie off the unit circle; taking the limit $c \to \infty$ means that the upper equilibrium state is a saddle focus, whereas the lower equilibrium is a real saddle. Therefore we can apply the theory of Knobloch & Wagenknecht [19] which shows that the branch of bright solitons must approach the heteroclinic cycle via a decaying oscillation in parameter space (a "*thin snake*"). In contrast, the lower equilibrium has real eigenvalues and so that grey soliton approaches the Maxwell point monotonically in P. The bifurcation diagrams for these bright and grey solitons are shown in Fig. 3.3(a),(b) . In fact, the presence of complex Floquet exponents (eigenvalues in the continuum limit) means that the standard theory of Shil'nikov homoclinic orbits to saddle foci (see, e.g. [27] or [17, 7] in a reversible context) shows that there must be infinitely many m-pulse orbits for *each* m sufficiently large in a neighbourhood of the Maxwell point. In what follows we shall not consider multi-pulse solutions further unless a discussion of them is important in the context of describing what happens to single-humped branches.

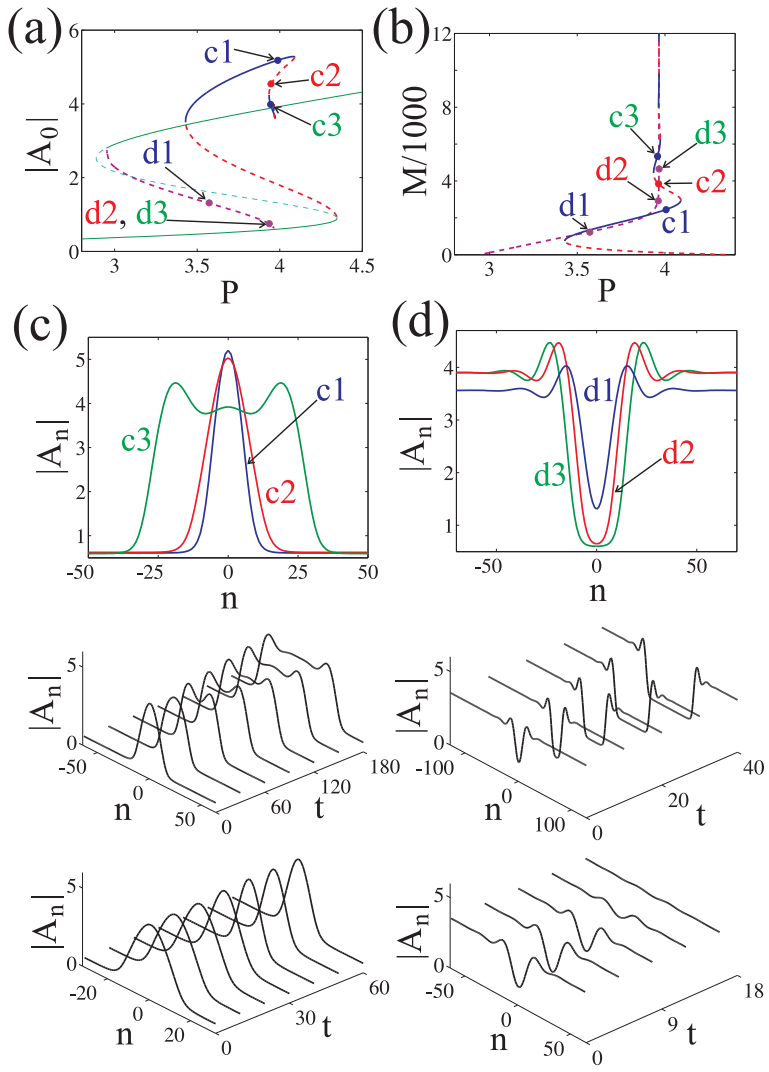

FIG. 3.3. *(a),(b) Bifurcation diagram of solitons against pump for* $\alpha = 10$, $\delta = -9.2 + 1i$ *and* $c = 12$. *The vertical axis in (a) is the absolute value of the central point, whereas in (b) it is the soliton mass given by (3.3). The thinner solid green and dashed cyan lines show the stable and unstable parts respectively of the homogeneous states. Solid blue and dashed red lines correspond to stable and unstable bright solitons respectively, whereas dashed magenta lines correspond to the grey soliton which is always unstable. In the upper part of panel (c) the field distributions are plot for three labelled points on the bright-soliton branch; points "c1" and "c3" are stable whereas "c2" is unstable. The two lower parts of the panel show temporal evolution under perturbations in the direction of positive or negative energy for this unstable case. Panel (d) similarly depicts three solutions on the grey-soliton branch, which are all unstable. The lower parts of the panel shows simulations of perturbations to the soliton labelled "d2".*

Let us consider the bifurcation diagram in Fig. 3.3 in more detail. Similarly to the conservative case, the branch of bright solitons continues to be born via a small-amplitude bifurcation at the right-hand fold point $P = P_+$. As P decreases, the soliton becomes narrower and more intense. For this part of the curve the soliton is unstable and thus corresponds precisely to the low-intensity soliton branch of Fig. 3.1.

Now though, instead of reaching zero pump, the bifurcation curve folds to the right (where the red and blue curve meet around $P = 3.5$ in panels (a) and (b)) and transforms into what was the stable higher-intensity soliton branch in the absence of dissipation. The branch then forms a thin snake around the Maxwell point, involving infinitely many folding points, with the width of the snake exponentially decreasing to zero with each successive fold. As the snake is traversed, the soliton gets wider and its mass M increases to infinity as the solution transforms into a pair of stationary fronts; which can be seen in Fig. 3.3(a) by the way the central part $|A_0|$ tends to the value $|A|$ of the upper homogeneous state as the snake is transversed.

The grey soliton branch does not exist in the conservative limit $\mathrm{Im}(\delta) = 0$. For the finite dissipation case shown in Fig. 3.3(a), it is born at the point $P = P_H$ where the upper homogeneous branch undergoes a modulation instability. Near this point, the soliton looks like a slow envelope function with a fast carrier field and may be described by the theory of sub-critical Hopf bifurcations in reversible systems (also known as a Hamiltonian-Hopf bifurcation or a 1-1 resonances see, e.g. [18, 6]). For higher P along the bifurcation curve, the soliton develops a deep central core as it approaches the heteroclinic connection to the lower homogeneous state. The width of the soliton tends to infinity as the pump approaches the Maxwell point, see the magenta lines in Fig. 3.3(a,b).

It turns out that the introduction of linear loss can stabilise the bright solitons but cannot stabilise the grey ones. This can be explained heuristically as follows. In the case of rather wide solitons, we can consider them as two fronts interacting through their tails. The decay of the soliton tails to the upper homogeneous states is oscillatory in the case with loss. Therefore, thinking of the bright soliton as a "bound state" of the two fronts, for pump values sufficiently close to the Maxwell point there are several equilibrium distances between the fronts that enable the formation of bright solitons. The interaction potential between the fronts depends on the distance between them, the equilibrium distances can be stable or unstable and neighbouring equilibria typically have opposite stability type (see e.g. [5] for a similar argument for a problem of fourth-order in space). For the grey solitons, however, the decay to the lower homogeneous state is governed by real eigenvalues and so there is unique distance between the two fronts close to the Maxwell point that gives rise to a bound state. This is the unique, monotonic-in-P branch of grey solitons which we find to always be unstable.

We find that each fold of the bright soliton snake connects a stable soliton to an unstable one. The development of the instability is shown in the middle and lower parts Fig. 3.3(c). In general, there may be three different scenarios: either the soliton splits into two fronts moving in opposite directions, (upper plot); or the two fronts may move towards each other and form a bound state (lower plot); or, given a sufficiently large perturbation, the two fronts may move towards each other and annihilate (not shown). The development of the instability for the grey soliton, which is shown in the middle and lower panels of Fig. 3.3(d), generally results in the formation of two fronts. If the fronts move in the opposite direction then the resulting state is two solitary fronts (upper plot), whereas if they fronts move towards each other they collide and annihilate (lower plot).

A key question remains. What happens to the grey soliton branch, the Maxwell point and the snaking curve of bright solitons as we decrease the loss from $\mathrm{Im}(\delta) = 1$ (Fig. 3.3) to the conservative case $\mathrm{Im}(\delta) = 0$ (Fig. 3.1 and Fig. 3.2) in which there are no such features?

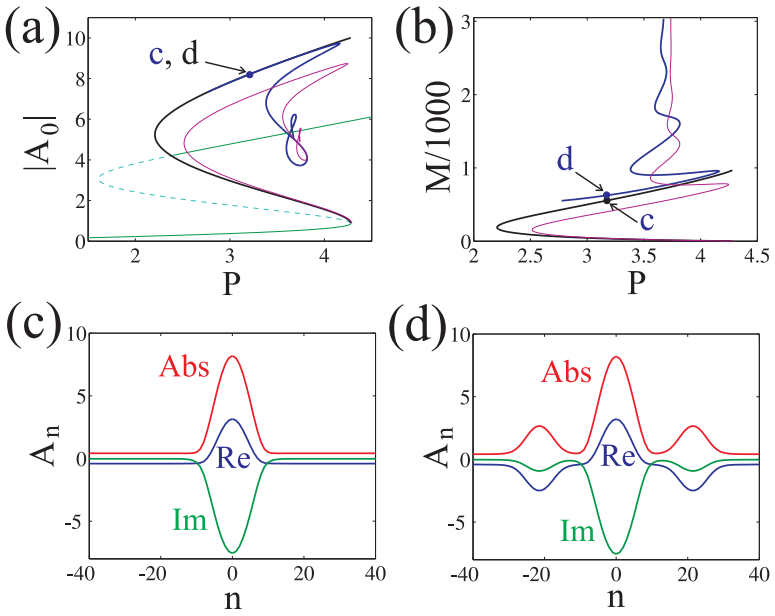

FIG. 3.4. *(a),(b) Similar to Fig. 3.3(a),(b), but for $\delta = -9.2 + 0.5i$. Black and blue lines lines show two distinct branches of bright solitons. Thinner magenta lines show how these two branches join for slightly higher loss, $\delta = -9.2 + 0.6i$. Thinner solid green and dashed cyan lines in panel (a) show the stable and unstable parts of the bifurcation diagram for the homogeneous states. The field distributions for the points marked as "c" and "d" in panels (a) and (b) are shown in panels (c) and (d) correspondingly.*

Consider first the bright solitons. As $\mathrm{Im}(\delta)$ decreases, the snake is destroyed by a sequence of codimension-two bifurcation. The first additional bifurcation to occur as we decrease $\mathrm{Im}(\delta)$ from 1 is that the rightmost folding point of the snake reaches the right-hand edge of the bistability region of the homogeneous state at $P = P_+$. As it does so the exponential rate of relaxation of the soliton's tails becomes weaker and weaker, until precisely at $P = P_+$, the decay becomes algebraic. For $\mathrm{Im}(\delta)$-values immediately below this first codimension-two bifurcation, the snaking curve now forms two separate pieces, see Fig. 3.4. One piece (shown by the black line) terminates as a large-amplitude algebraically decaying soliton at $P = P_+$ just like the blue curve in Fig. 3.1. The other piece (shown by a blue line) does not quite reach the right-hand edge of the bistability region, but instead continues to snake towards the Maxwell point with ever increasing mass M. If we follow this curve with decreasing M though, the branch now connects to a curve of three-humped multi-pulses that begins to track the single-pulse branch closely albeit for 3 times its M-value (for convenience, to avoid an overly cluttered bifurcation diagram we have terminated the computation of this branch artificially around $P = 2.8$). The fact that solutions on this branch for lower P-values become increasingly like a three-pulse soliton can be seen by comparing the solution graph at the point labelled "d" (Fig. 3.4(d)) with the single-hump solution at the same P-value (panel (c)).

As we continue to decrease $\mathrm{Im}(\delta)$, then further splitting of the snaking bifurcation curve happens, see Fig. 3.5 where there are three branches of bright solitons, shown by black, blue and red curves. This splitting is slightly different to the one illustrated in Fig. 3.4 in that it does not happen at $P = P_+$, but via a transcritical bifurcation

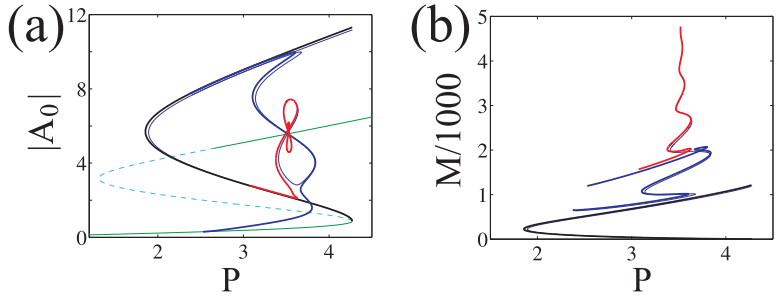

FIG. 3.5. *(a),(b) Similar to Fig. 3.4(a),(b), but for* $\delta = -9.2 + 0.4i$. *Black, blue and red lines show three distinct branches. Thinner blue lines show how the red and blue curves join for slightly higher loss* $\delta = -9.2 + 0.41i$.

between the snaking curve and a curve that connects two multi-pulses *within* the bistability region. Thus a new closed branch is created that connects two different multi-pulse solutions in the conservative limit (like the blue curve in Fig. 3.2). The snake now connects to a new branch of multi-pulses with higher mass M. We conjecture that there are in fact infinitely many such splittings of the snake as the loss is further reduced. Figure 3.6 shows an approximate calculation of the Maxwell point $P = P_M$, the two folds $P = P_\pm$, and the modulation instability of the upper branch as P and $\mathrm{Im}(\delta)$ vary. As can be seen, the Maxwell point moves to lower P-values and seems to disappear altogether at around $\mathrm{Im}(\delta) = 0.35$ by which loss-value the last remnants of the bright-soliton snake must disappear altogether.

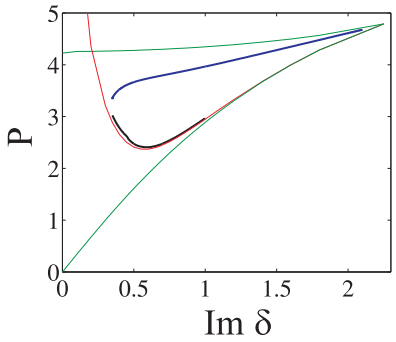

FIG. 3.6. *An approximate two-parameter diagram showing the boundaries of the region of bistability region* $P = P_\pm$ *(green line) and the modulation instability* $P = P_H$ *(red line) as a functions of the losses* P *and* $Im(\delta)$. *Also plotted are approximate computations of the positions of the Maxwell point between the two homogeneous states (blue line) and a curve (black line) on which the width of the grey soliton is equal to a fixed constant 11.5. This wide soliton is part of the small amplitude branch that bifurcates subcritically at* $P = P_H$. *The other parameters are held fixed at* $Re(\delta) = -9.2$, $\alpha = 10$ *and* $c = 12$.

Now let us consider what happens to the grey solitons as the loss is reduced. Figure 3.6 provides numerical evidence that the Maxwell point disappears by colliding with the modulation instability curve, when $P = P_H = P_M$ for $\mathrm{Im}(\delta) \approx 0.35$. That is, at such a value of the loss, the point of small-amplitude birth of the grey solitons and their point of destruction via a heteroclinic connection occur at the same P-value. Thus we might conjecture that as $\mathrm{Im}(\delta)$ is decreased towards 0.35, the curve of grey solitons becomes steeper and steeper when plot as M against P, occupying

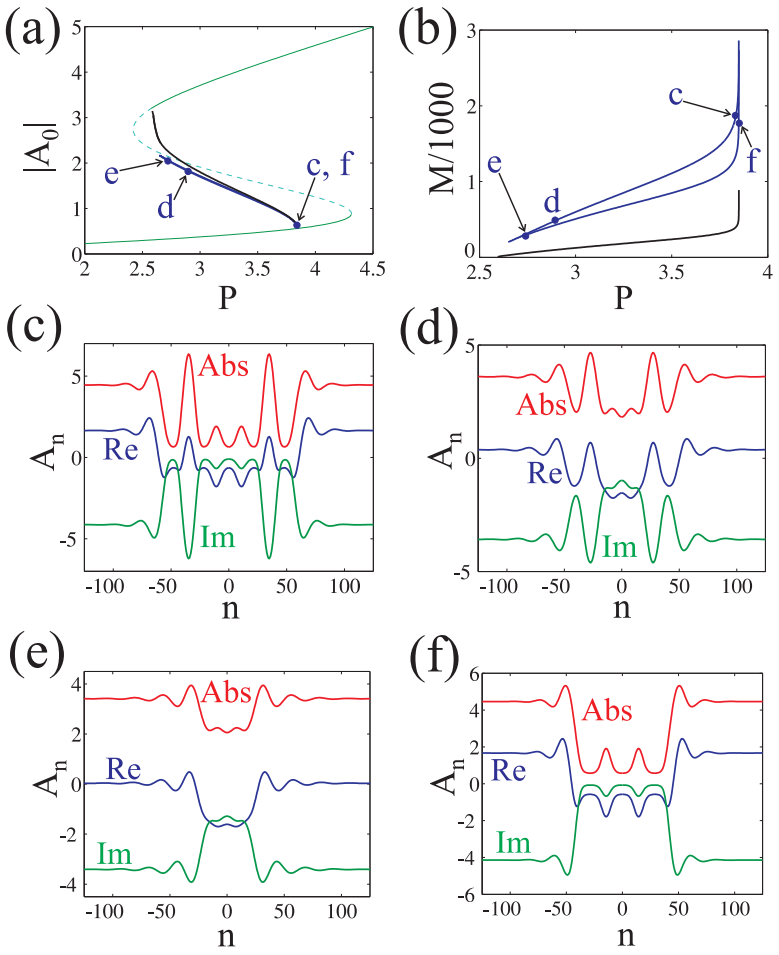

FIG. 3.7. *Similar to Fig. 3.5, but for grey solitons when* $\delta = -9.2 + 0.8i$. *The branch of single-pulse grey solitons is shown by a black line, and the blue line shows an isola of multi-pulse solitons. The field distribution for the points labelled "c", "d", "e" and "f" in panels (a) and (b) are shown in panels (c)-(f) correspondingly. For slightly lower loss values, the isola and the single-pulse branch interact via a transcritical bifurcation.*

a smaller and smaller interval of P-values, until it eventually disappears altogether. Our numerical computations suggest that, while broadly speaking this explanation appears to hold, the precise details are more complex. For example, Fig. 3.6 plots a curve of grey solitons of fixed "width" close to their bifurcation from P_H. Note that as $\mathrm{Im}(\delta)$ is reduced towards 0.35, the wide solitons seems to occur further from P_H rather than closer to it. This provides indirect evidence that for some nearby loss-value the spatial Hopf bifurcation at P_H changes from being subcritical to supercritical. Such a mechanism can occur in two ways depending on the sign of the next-order term in the normal form; either via the formation of a local small amplitude Maxwell point to a periodic state [30], or via the homoclinic orbit becoming wider and wider and eventually detaching from the local bifurcation altogether [13]. The numerical evidence presented here suggests that the latter case applies. Thus the global topology of the grey soliton branch becomes more complex as the branch becomes thinner

and appears to involve further transcritical bifurcations with other multi-pulse states that are shown in Fig. 3.7 (for higher loss values where the primary and multi-pulse branches are still distinct).

3.3. Discrete solitons. Let us now address the effect of discreteness on the solitons, which we achieve computationally by allowing c to become much lower. In general, each branch of continuum localised solutions has two counterparts in the discrete case, one symmetric under reversibility R_1 (a so-called on-site solitons), the other symmetric under R_2 (off-site solitons).

We shall deal first with the bright solitons. Bifurcation diagrams for the on-site and off-site discrete cavity solitons are shown in Fig. 3.8. Note that both families form snaking patterns around what was the Maxwell point, which can be seen from the field distributions in Fig. 3.8(d) to occur because of a heteroclinic connection to the upper homogeneous state. Note here a clear distinction from the continuum case, in that we have *wide snakes*. That is, the width of the snakes now do not decrease to zero as the mass increases to infinity, but tend to a fixed finite width. The interval of P-values between which the snaking occurs represents the so-called *pinning region* [26, 4] at which there is a heteroclinic connection between the upper and lower homogeneous states. The shape of the branches of snaking curves in this case can be predicted by an understanding of how the stable and unstable manifolds of the heteroclinic cycle unfold, see [30, 11, 2].

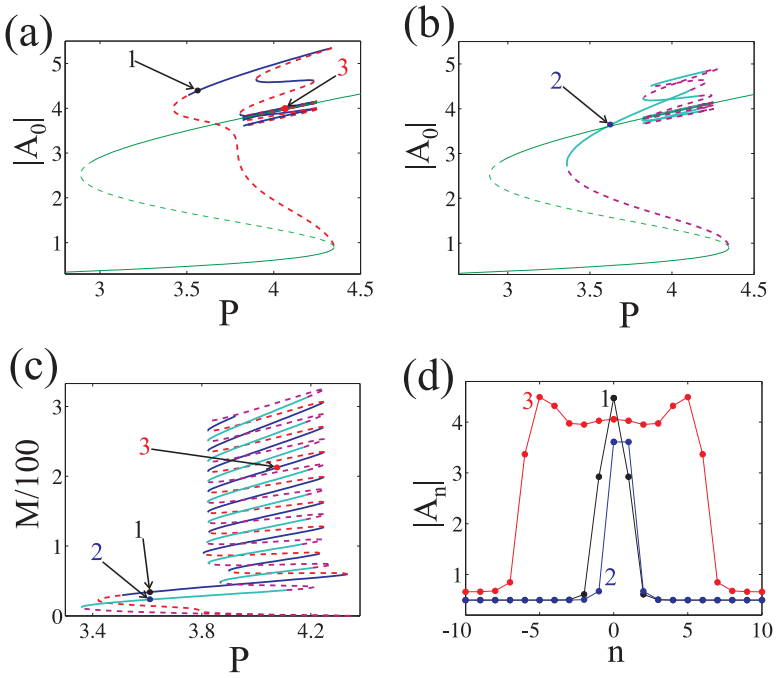

FIG. 3.8. *Similar to the bright-soliton curves in Fig. 3.3 but in the discrete case with* $c = 0.5$. *Panel (a) shows on-site solitons and (b) shows off-site solitons; both are overlaid in panel (c). Solid lines (blue and cyan) represent stable parts of the bifurcation curves, whereas dashed lines (red and magenta) represent unstable parts. Field distributions corresponding to the points labelled "1", "2" and "3" are shown in panel (d)*

We have also studied the stability of the bright solitons and found this to be some-

what more complicated than in the continuum case $c \to \infty$, but nevertheless to be in line with the theory [3, 2] for snakes that approach heteroclinic connections between equilibria and periodic orbits in continuum systems. For both the on-site and off-site solitons, after each second successive fold of the snaking curve the branch becomes stable. Close to each fold point, there is an additional pitchfork bifurcation that gives rise to a loss of stability slightly away from the fold point (this is most noticeable for the right-hand folds of the off-site solitons). These represent symmetry-breaking bifurcations which cause the formation of non-symmetric solitons along branches that connect the pitchforks on two branches with opposite symmetry. These are the "ladders" in the theory of Burke and Knobloch [4]. We omit their computation here, as we have found no numerical evidence to suggest they are temporally stable (cf. the rigorous theory of [2] in the case of continuum systems). However, we do note one interesting feature from Fig. 3.8(b),(c) that (at least for the off-site solitons) the symmetry-breaking bifurcations occur on the "stable" side of each saddle node, which is not the same orientation that was previously observed in [3]. The typical development of the temporal instability along the unstable part of the symmetric branches in Fig. 3.8 leads to the splitting of the solitons into a pair of moving fronts. In the case when the fronts move toward each other they can collide and annihilate as a result of the collision.

The "width" of the snake (in P) depends crucially on the other parameters in the problem; see Fig. 3.9 which shows various two-parameter bifurcation diagrams with variation of P and another parameter. Panels (a) and (b) show what happens as the coupling strength varies. Note that the snake becomes progressively narrower as c increases, reaching in the continuum limit $c \to \infty$ the so-called thin snakes that we encountered in Sec. 3.2. In fact, the figure shows that $c \geq 2$ is already a good numerical approximation to the continuum limit for these parameter values, thus justifying our earlier use of $c = 3$ as an approximation to that limit. The figure also illustrates another phenomenon as c becomes too small. For slightly lower c-values than those depicted, the right-hand side of the snake (the red curve in Fig. 3.9(b)) approaches the (black) boundary of the bistability region. We shall describe in detail the implications of such a codimension-two bifurcation shortly.

The remaining panels of Fig. 3.9 show how the one-parameter snaking bifurcation diagrams depend on damping $\mathrm{Im}(\delta)$ (panels (c) and (d)) and on detuning $\mathrm{Re}(\delta)$ (panels (e) and (f)). In both cases observe that there is a limit (obtained by increasing $\mathrm{Im}(\delta)$ or decreasing $\mathrm{Re}(\delta)$ in which the bistability region vanishes. At such a point the right-hand and left-hand folds of the homogeneous state annihilate each other in a codimension-two cusp bifurcation. The continuation of the right and left-hand edges of the snaking curve shows that as the bistability region gets thinner, the snake gets thinner much more rapidly. Note though the numerical difficulties we had in computing these folds right up to the cusp. Nevertheless a natural conjecture would be that the snake survives all the way up the cusp but becomes "exponentially thin" in this limit, just as it is in the neighbourhood of a codimension-two degenerate Hamiltonian Hopf point [20]. An unfolding of such a beyond-all-orders bifurcation remains beyond the scope of the present work.

Now let us discuss what happens to these bright discrete solitons as the right-hand limit of the snaking curve approaches the edge of the bistability region. We shall focus on the case illustrated in Fig. 3.9 in which this transition happens as we decrease $\mathrm{Im}(\delta)$. The first bifurcation occurs at some critical loss value where the rightmost (low M) fold point of the snake reaches the parameter value $P = P_+$ of the right-hand fold

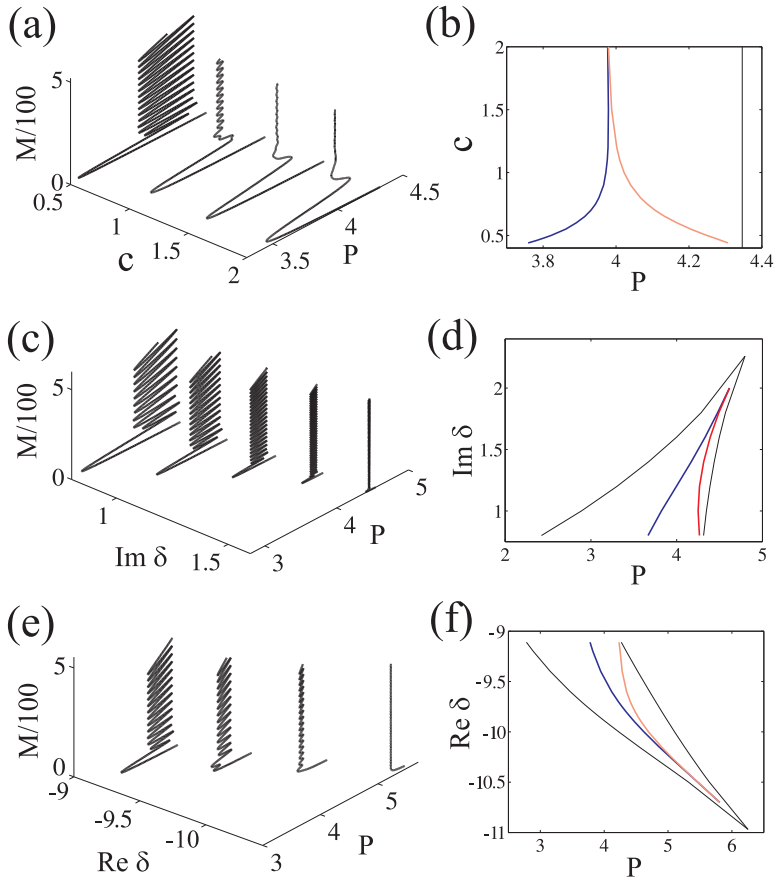

FIG. 3.9. *Two-parameter bifurcation diagrams of bright solitons for* $\alpha = 10$. *Panels (a), (c) and (e) show one-parameter slices through the three-dimensional bifurcation diagrams with norm* M. *Panels (b), (d) and (f) show the two-parameter bifurcation loci of the limiting folds of the solitons for high* M*; blue line for the left-hand folds and red line for the right-hand ones. The thin black lines on these plots show the (fold bifurcation) boundaries of the bistability stability region of the homogeneous states. The other parameter values used are: (a),(b)* $\delta = -9.2 + i$*; (c),(d)* $c = 0.5$, $Re(\delta) = -9.2$*; ; (e),(f)* $c = 0.5$, $Im(\delta) = 1$.

of homogeneous state. At such a point, just like in the continuum limit, we have an algebraically-decaying large-amplitude solitary wave. For lower losses, the bifurcation diagram splits into two parts; see Fig. 3.10(a). The upper part continues to snake, the lower part folds once and terminates as an algebraically decaying soliton at $P = P_+$. At some yet smaller $\mathrm{Im}(\delta)$-value another fold of the snake reaches P_+ and a second splitting happens; see Fig. 3.10(b). These are the first two in a subsequently chain of splitting bifurcations that happen for a small interval of $\mathrm{Im}(\delta)$-values as the former snake splits into infinitely many parts. Each part consists of a *loop* in parameter space that connects a soliton of "width" N (that is with N high intensity states in the core of the soliton, c.f. Fig. 3.8(d)) to an $N+2$-width soliton. The ends of the loop terminate at $P = P_+$ where the soliton's tails become algebraically decaying. This infinite family of loops survives all the way down to the conservative limit $\mathrm{Im}(\delta) = 0$. The lowest part of the bifurcation curve then corresponds to the one-pulse soliton, and the other loops correspond to different bound states of this one-pulse.

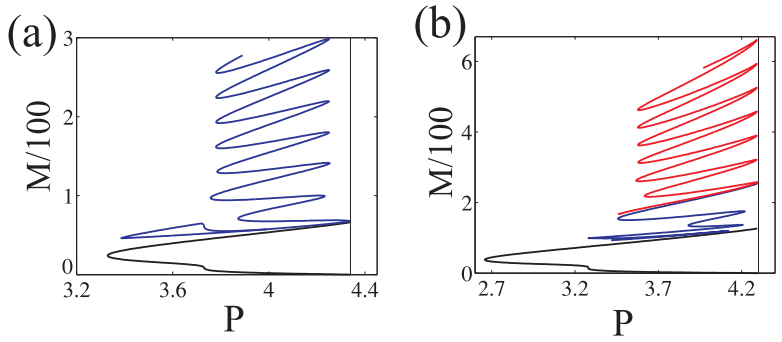

FIG. 3.10. *Similar to Figs. 3.4 and 3.5 but for (a) $\delta = -9.2 + 0.95i$ and (b) $\delta = -9.2 + 0.65i$. Different colours correspond to different branches of the bifurcation curve. The thin vertical line shows $P = P_+$, the right-hand edge of the bistability region*

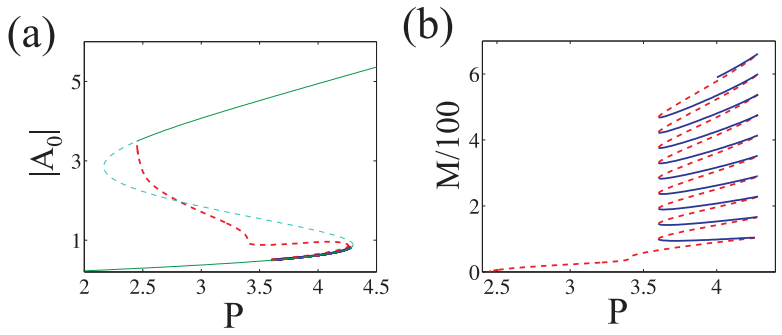

FIG. 3.11. *Similar to Fig. 3.8 but for on-site grey solitons and with $\delta = -9.2 + 0.7i$. Blue solid lines show the stable parts of the bifurcation curves, red dashed lines show the unstable parts. The solid parts of the curve correspond to the stable homogeneous states and the dashed part of the curve corresponds to the unstable states. The parameters are $\alpha = 10$, $\delta = -9.2 + 0.7i$ and $c = 0.5$.*

For the grey solitons, the presence of discreteness also leads to the formation of snaking bifurcation curves, see Fig. 3.11 (which depicts just the on-site case, bifurcation curves for off-site solitons are similar). We found by spectral computation and by direct numerical simulations that discreteness can also stabilise the grey solitons. Heuristically this stabilisation is because the discretisation forms an effective periodic potential for the fronts whose bound states form the solitons. The stability properties of the branch are similar to those of the bright solitons, that is, stability changes at or near each fold of the snake.

If the loss is decreased then the bifurcation diagram for the grey solitons also undergoes splitting into infinitely many parts as the rightmost fold of the snake reaches $P = P_+$. However, this mechanism is rather different than it was for the bright solitons. For the grey solitons, the homogeneous state undergoing the fold at P_+ is the state that forms the *core* of of the grey soliton at the Maxwell point, rather than its tail. Therefore the tails of the grey solitons continue to be exponentially decaying as they approach this boundary, and there is no contradiction in grey solitons existing for $P > P_+$. Nevertheless we find that the grey snake is destroyed as it approaches this boundary, albeit in a more complicated way than for the destruction of the bright soliton snakes considered above, see Fig. 3.12. Specifically, as each successive right-hand fold of the snake approaches the bistability region, it forms a transcritical

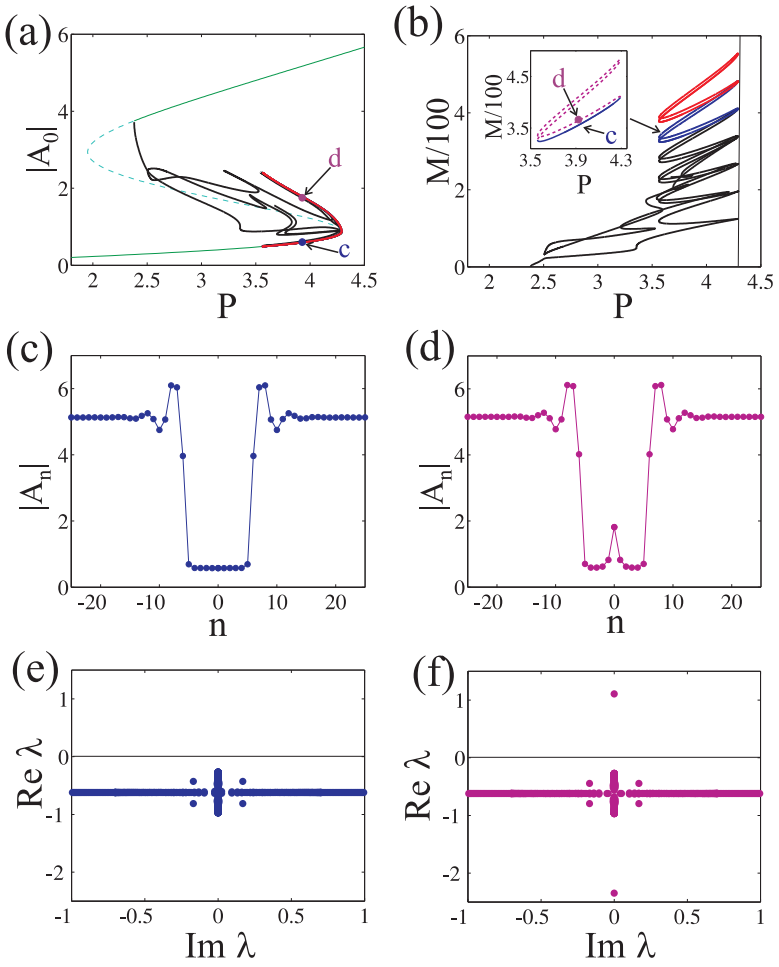

FIG. 3.12. *(a),(b) Similar to Fig. 3.11 but for slightly lower loss* $\delta = -9.2 + 0.6i$. *Black, blue and red line correspond to the lower, the second and the third branches of the bifurcation curve. The inset shows the second branch of the bifurcation curve in more detail, here solid lines correspond to stable solitons and dashed lines to unstable. The field distributions corresponding to the points labelled "c" and "d" are shown in the corresponding panels. Panels (e) and (f) show eigenvalues governing the stability of the solitons at the same two points. Note that here the real part of the eigenvalues are on the vertical axis, and the imaginary part on the horizontal axis.*

bifurcation with another branch of solitons, so that the global bifurcation diagram changes its topology. What results are infinitely many closed bifurcation curves, or *isolas* that form an approximate double covering of a C-shaped curve when plot as M against P. As we traverse one of these isolas we see that the a piece of the former grey soliton snake has now connected to a branch of more complex states that represent a grey soliton with an additional bright soliton residing in its core. Note that close to P_+, the bright soliton has much smaller amplitude than the grey soliton (compare graphs of one and two-pulse solitons in Fig. 3.12(c) and (d)). We found that a portion of the single-pulse part of each isola is stable, whereas the complexes formed with an additional central bright soliton are always unstable. Clearly, the precise topology of how these isolas are formed and metamorphose as one decreases $\mathrm{Im}(\delta)$ is a highly

involved process.

3.4. Larger detuning. We have so-far considered solitons with linear detuning that is sufficiently weak so that at zero pump $P = 0$, in the absence of dissipation, they can be compensated by the nonlinear correction to the resonance frequency. As we saw in Sec. 2.1, slightly larger detuning can still allow for a bistability region to occur, specifically if $-9\alpha/8 < \delta < -\alpha$. Preliminary results for this case were announced in [32]. Starting from the continuum limit in the absence of dissipation, we restrict attention to stationary pure real solutions to (3.1). Such solution trajectories in the (A, A_X) phase plane correspond to motion of a particle in the potential F given by (3.2).

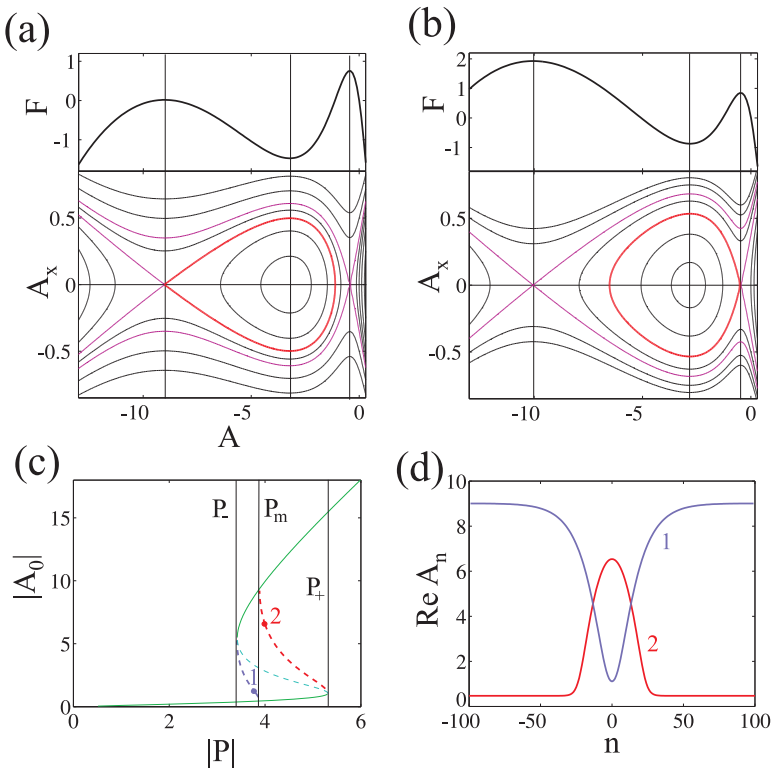

FIG. 3.13. *Similar to Fig. 3.1 but for $\alpha = 10$, $\delta = -10.3$ and $c = 25$. The potential F and the corresponding phase plane are shown in panel (a) for $P = 3.8$ and in panel (b) for $P = 4$. Magenta lines show the seperatrices of the saddle points, with the thicker red lines picking out the homoclinic trajectories, which correspond to solitons. Panel (c) shows a bifurcation diagram where the dashed blue line represents the grey soliton, the dashed red line shows the bright soliton and the solid and dashed green lines show the stable and unstable homogeneous states respectively. The homoclinic trajectories shown in (a) and (b) corresponds to the points "1" and "2" on the bifurcation curves, their field are shown in panel (d).*

In the region of bistability $P \in (P_-, P_+)$ the potential has three extrema which, unlike the previous case, represent two maxima (corresponding to the lower and the upper homogeneous states) and a minimum (corresponding to the intermediate state); see Fig. 3.13. In this case, we have a Maxwell point even for the continuum, conservative problem; this occurs at the value $P = P_M$ where the two maxima have the same value of the F.

For pump values below the Maxwell point, specifically $P \in (P_-, P_M)$, a homoclinic connection occurs to the upper homogeneous state (see Fig. 3.13(a)), which represents a grey soliton. The soliton is born at low amplitude at $P = P_-$, the left-hand fold point of the homogeneous states. As the pump is then increased the soliton's mass increases, while the central point A_0 decreases. As the pump approaches the Maxwell point, the core of the grey soliton gets closer to the low-intensity homogeneous solution, and therefore its profile becomes much wider. Exactly at the Maxwell point the homoclinic orbit becomes a heteroclinic cycle representing two stationary fronts that connect the upper and the lower homogeneous states. If the pump exceeds the Maxwell point, specifically $P \in (P_M, P_+)$, then the heteroclinic trajectories splits into a homoclinic orbit to the low-intensity homogeneous state. This trajectory corresponds to a bright soliton. As the pump is further increased, the bright soliton disappears in a small-amplitude bifurcation at $P = P_+$, just as it did in the case for smaller detuning. Direct numerical simulations and the spectral analysis of linear stability reveal that both grey and bright solitons are unstable throughout the region of bistability (despite the fact that the homogeneous states in their tails are both temporally stable).

Fig. 3.14 presents the bifurcation diagram for solitons still in the continuum limit, but with added dissipation. Note that this diagram is qualitatively similar to the corresponding figure with smaller detuning, Fig. 3.3. Now, windows of stability have opened up inside the bright soliton branch, as it undergoes a thin snake around the Maxwell point. This snaking behaviour is because the spatial eigenvalues of the upper homogeneous state have nonzero imaginary part.

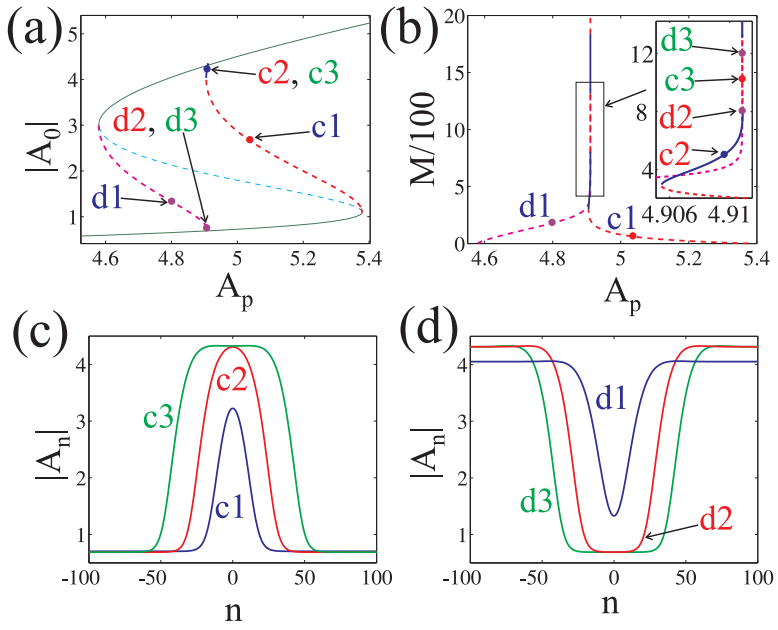

FIG. 3.14. *Similar to Fig. 3.13(c) but with the introduction of linear loss* $Im(\delta) = 0.8$. *Grey solitons are represented by the dashed magenta line and bright solitons by solid blue (stable) and dashed red (unstable) lines. The field distributions for the points marked "c1"-"c3" and "d1"-"d3" are shown in panels (c) and (d) correspondingly.*

Adding the effect of discreteness causes both the bright and grey solitons to undergo thick snaking bifurcation diagrams, just as it did for smaller detunings. Results

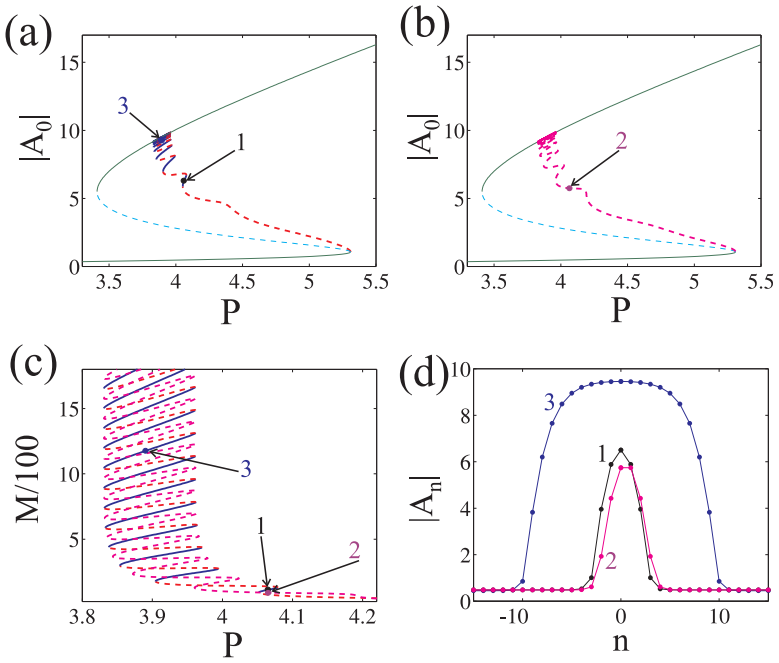

FIG. 3.15. *Bifurcation diagrams of on-site (blue and red curves), and off-site (magenta) bright solitons for* $\alpha = 10$, $\delta = -10.3$ *and* $c = 0.5$. *Solid lines represent stable solutions, and dashed lines unstable ones. Graphs of solutions at points labelled "a", "b" and "c" are shown in panel (d).*

are presented for bright solitons in Fig. 3.15. One difference with the previous case is that for these parameter values the off-site solitons are always unstable (cf. Fig. 3.3). Grey solitons behave similarly (see Fig. 3.16(a)). Another key difference from the case for smaller detuning is that for $-9/8\alpha < \mathrm{Re}(\delta) < -\alpha$ the bifurcation curves vary smoothly when we decrease $\mathrm{Im}(\delta)$, since the Maxwell point survives right down to the conservative limit. Also, as with the case of smaller detunings (cf. Fig. 3.6), as loss is increased, the width of the bistability region for homogeneous states starts to shrink, so that there is an upper threshold of $\mathrm{Im}(\delta)$ for which the two folds $P_\pm$ come together in a cusp point and the bistability region disappears altogether. Nevertheless we find that the Maxwell point and therefore the branches of bright and grey solitons survive all the way up to this point. However, the width of the snaking part of the bifurcation diagram decreases with loss much faster than the bistability region of the homogeneous state, see Fig. 3.16. Panels (a) and (b) show the cases of no loss and moderate loss respectively, suitably scaled so as to show the relative width of the snaking area to the width of the bistability region. As a result of such behaviour, the folding points of the snake can never reach the edge of the bistability region and so the snake does not undergo any splitting.

4. Solitons for defocusing nonlinearity. In this section we concentrate on solitons in the case of sufficiently small detuning $0 < \delta < -\frac{9}{8}\alpha$. As we did for focusing nonlinearity, let us start the consideration from the continuum limit $c \to \infty$

4.1. Conservative case in continuum limit. When α and δ are both real, there is once again an invariant subspace in which A is pure real, within which we can study the problem using phase plane analysis; see Fig. 4.1. When $P = 0$, there is

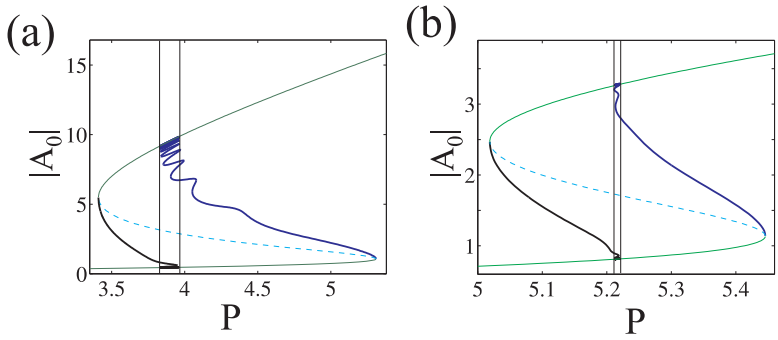

FIG. 3.16. *Bifurcation diagrams of bright and grey solitons for* $\alpha = 10$, $c = 0.5$ *and (a)* $\delta = -10.3$, *(b)* $\delta = -10.3 + 1.1i$. *Black and blue lines correspond to grey and bright solitons respectively.*

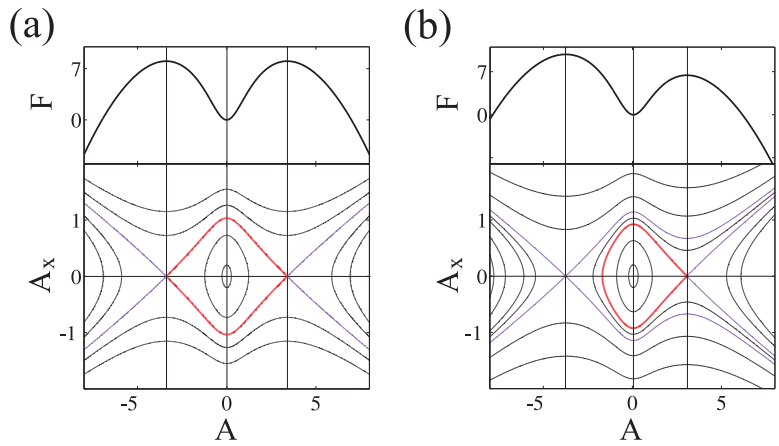

FIG. 4.1. *The potential* F *given by (3.2) and the corresponding phase planes for alpha* $= -10$, $\delta = 9.2$ *and (a)* $P = 0$, *(b)* $P = 0.5$. *Thicker red lines show the trajectories corresponding to the fronts and solitons, the other seperatrix trajectories are shown by magenta lines. The black lines show the other trajectories.*

a stationary front connecting the two homogeneous states whose phases differ by π. Such a front is sometimes known in the physics literature as a "*topological soliton*" (or indeed as a "dark soliton" in the context of NLS equations) as it passes through the phase singularity at $A = 0$. On the phase plane this front corresponds to a heteroclinic trajectory connecting two saddle points. So the bifurcation curve for the soliton starts at zero pump at infinite M. As the pump increases, the tail of the soliton connects to the intermediate homogeneous state and disappears at small amplitude at the right-hand fold point $P = P_+$ of the homogeneous states; see Fig. 4.2 (the snaking of the bifurcation curve for small P in the figure is a consequence of the large but finite discreteness. Note that $c = 15$ is no longer a good approximation to the continuum limit for small P. Nevertheless we have verified numerically that this snake becomes progressively more like a pure vertical asymptote at $P = 0$ in the P versus M diagram in the limit $c \to \infty$).

These results would appear to be a contradiction to Proposition 2.1, since the intermediate state is not temporally stable, yet we see a branch of solitons that connect

to it, which would suggest that the spatial dynamics is hyperbolic. The resolution of this apparent contradiction is that the soliton is pure real, and the invariant subspace in which A is real contains only the hyperbolic directions of the linearisation around the intermediate homogeneous state. The centre manifold in which the imaginary spatial eigenvalues reside is orthogonal to this invariant subspace. The existence of these centre directions means that these topological solitons (which could be more accurately described as grey solitons for $P > 0$) can never be temporally stable and therefore are of little physical significance.

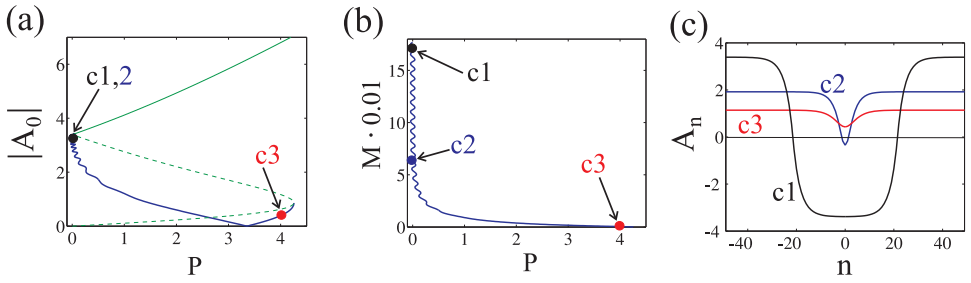

FIG. 4.2. *Bifurcation diagram for the "topological" on-site conservative soliton as a function of the pump P, for $\delta = 9.2$, $\alpha = -10$, and $c = 15$. The thick blue line corresponds the solitons and the thin green line shows the homogeneous states, with a dashed line representing instability. The bifurcation diagrams showing the dependencies of M on the pump is shown in panel (b). (c) The field distribution of the solitons for three labelled points.*

4.2. The effect of loss and discreteness. Another reason why the topological soliton branch in Fig. 4.2 is of limited physical interest, is that introducing small losses $\mathrm{Im}(\delta) > 0$ immediately destroys the branch. This is because real-A is no longer an invariant subspace and so any solitons would have to connect to a saddle-centre equilibrium. From the theory of embedded solitons we know that connections to such states are of codimension-one at best (see e.g. [9]). Instead, we see nearby generic families of homoclinic trajectories that connect to small-amplitude limit cycles around the saddle-centre equilibrium point. Note that the upper homogeneous branch (the solid green line Fig. 4.2) *is* fully temporally stable (spatially hyperbolic) but, as we can see from Fig. 4.1(b), there is no homoclinic connection to this branch for $P > 0$ in the conservative case. Therefore, we find that there is no continuation of the conservative topological solitons into pumped, damped media with defocusing nonlinearity.

Nevertheless, introduction of sufficiently large losses can create branches of both bright and grey solitons, the typical bifurcation diagrams for which are shown in Fig. 4.3, which is in the discrete case of finite c. The branch of bright solitons (shown as a red line) is born at a modulation instability of the lower homogeneous state and terminates at a Maxwell point for a lower pump value. Note that the location of the modulation instability and the Maxwell point tend uniformly to $P = 0$ as $\mathrm{Im}(\delta) \to 0$. For higher loss values than those depicted in Fig. 4.3, the modulation instability reaches the right-hand fold at $P = P_+$ and the lower homogeneous state then is always stable. For this and higher values of $\mathrm{Im}(\delta)$, the bright soliton branch is born at the right-hand fold. The bright solitons are always unstable in the continuum limit because the decay to the upper homogeneous state is monotonic and so there is no (thin) snake that opens up windows of stability. Introduction of discreteness (finite c) can stabilise these solitons in the usual way, through the transformation into a snaking bifurcation diagram in a neighbourhood of the Maxwell point.

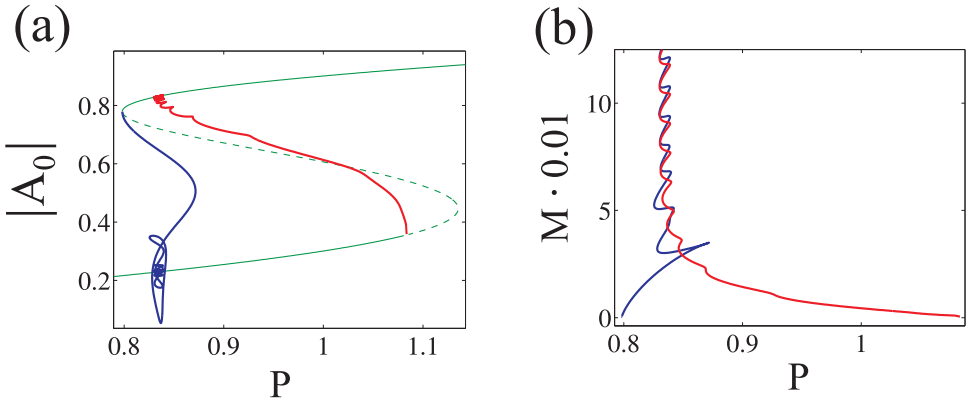

FIG. 4.3. *Bifurcation diagrams of bright (red line) and grey (blue line) on-site cavity soliton as the pump P varies for $\delta = 4 + 1i$, $\alpha = -10$, and $c = 1$. The thin green lines shows the bifurcation diagram of the homogeneous states*

Also shown in Fig. 4.3 (as a blue line) is a branch of grey solitons, which detaches from the left-hand fold of homogeneous states at $P = P_-$ before reaching the Maxwell point.

Figure 4.4 shows the branch of grey solitons for larger detuning, smaller loss, and large c. One can see that the bifurcation diagram has a quite complicated structure. It would appear that at these parameter values the soliton is close to connecting to a periodic orbit in its core, but eventually it snakes in P around the Maxwell point of the homogeneous state as the amplitude of the oscillations decrease for very large M.

Notice from Fig. 4.4 that the leftmost folds of the snake are close to the left-hand edge of the bistability region $P = P_-$. For slightly higher loss-values, we find that the first of these folds touches the edge of the bistability region, see Fig. 4.5. The scenario is like that which occurs for bright solitons with focusing nonlinearity (see, e.g. Fig. 3.10) where it is the homogeneous state in the *tail* of the soliton that undergoes the fold. This touching leads to a global bifurcation where the lower part of the snake splits off into a separate loop. A sequence of bifurcations then ensues which converges rapidly as the loss is further increased, in which the entire snake splits into similar closed loops. One distinction with the case of bright solitons for focusing nonlinearity though is that in this case, there is a second much higher threshold of $\mathrm{Im}(\delta)$ at which the reverse process happens. That is the loops reform into a snake as $\mathrm{Im}(\delta)$ is increased, see Fig. 4.6.

An interesting feature of the new snake that is formed for these much higher loss values is that, even in the continuum limit, we have a wide snake; see Fig. 4.7. This is because the soliton does not snake around a Maxwell point at which there is a heteroclinic connection to a homogeneous state (an equilibrium point of the spatial dynamics in the continuum limit). Instead the snake forms around a heteroclinic connection between the tail equilibrium state and a large amplitude periodic state. This is much more akin to the kind of snaking bifurcation diagrams that are found in the Swift-Hohenberg equation [4, 3].

Finally, we discuss what happens to these structures as we increase discreteness. Specifically Fig. 4.8 shows what happens as c is progressively decreased for the parameter values used in Fig. 4.7. In particular, the discreteness introduces a second "frequency" into the bifurcation diagram and we observe a kind of quasi-periodic

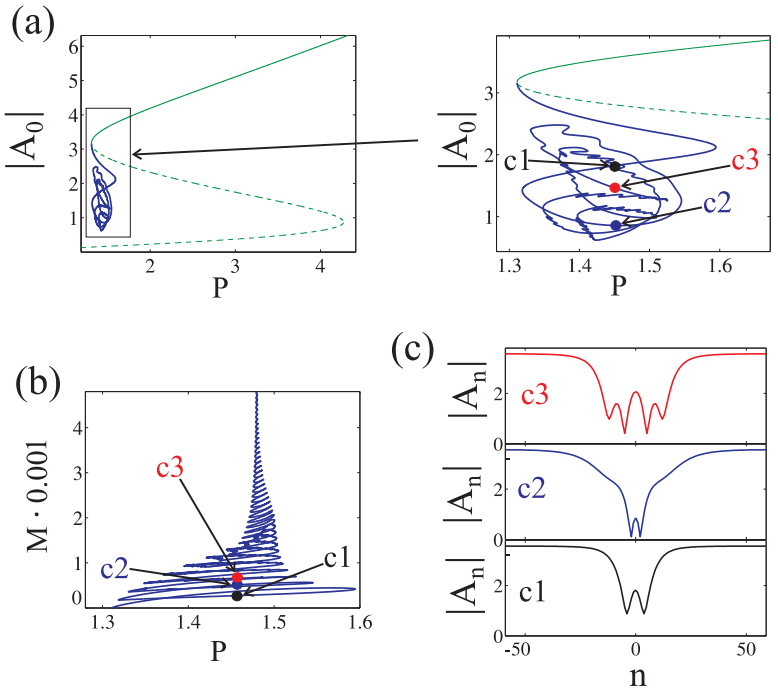

FIG. 4.4. *(a), (b) Similar to Fig. 4.3 but for* $\delta = 9.2 + 0.4i$, $\alpha = -10$, *and* $c = 15$. *(c) The field distribution of the solitons for the three labelled points.*

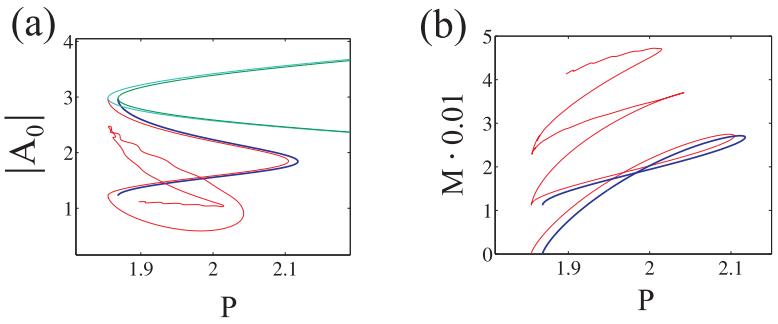

FIG. 4.5. *(a) Similar to Fig. 4.4(a) but for* $\delta = 9.2 + 0.59i$. *In addition, thin red and cyan lines show a part of the same bifurcation curves but for a slightly lower loss-value* $\delta = 9.2 + 0.585i$. *The other parameters are* $\alpha = -10$ *and* $c = 15$. *(b) The same scenario plot as* P *versus* M

snaking structure in which additional small loops occur; see panel (a) of the Fig. 4.8, which is for $c = 2.75$ and its blow-up in panel (b). As the coupling strength is further decreased, the loops grow, and there seems to be a complex interplay between the main limbs of the snaking curve and the loops; see panels (c) and (d) of Fig. 4.8 which are for $c = 2$ and $c = 1$ respectively. For sufficiently low coupling the snaking diagram becomes regular again; see panel (e), which is for $c = 0.5$, and the corresponding graphs of solutions in panel (f), which now look quite different from their "smooth" counterparts in Fig. 4.7(c). Clearly the transformation that occurs as we pass from the continuum limit to the fully discrete problem in this case is highly involved and a complete investigation is beyond the scope of this paper.

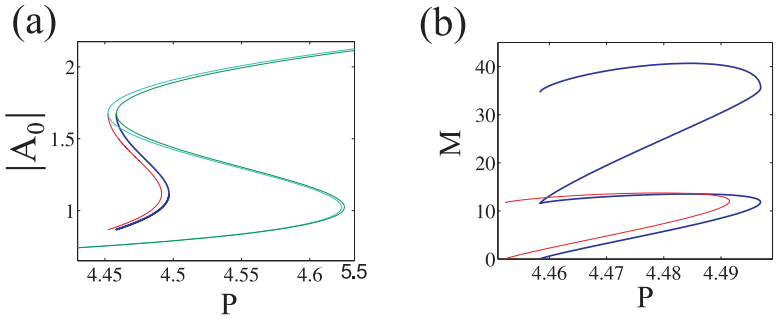

FIG. 4.6. *Similar to Fig. 4.5 but for (thin green and red lines)* $\delta = 9.2 + 1.935i$ *and (thick blue and green lines)* $\delta = 9.2 + 1.93i$. *The other parameters are* $\alpha = -10$ *and* $c = 15$.

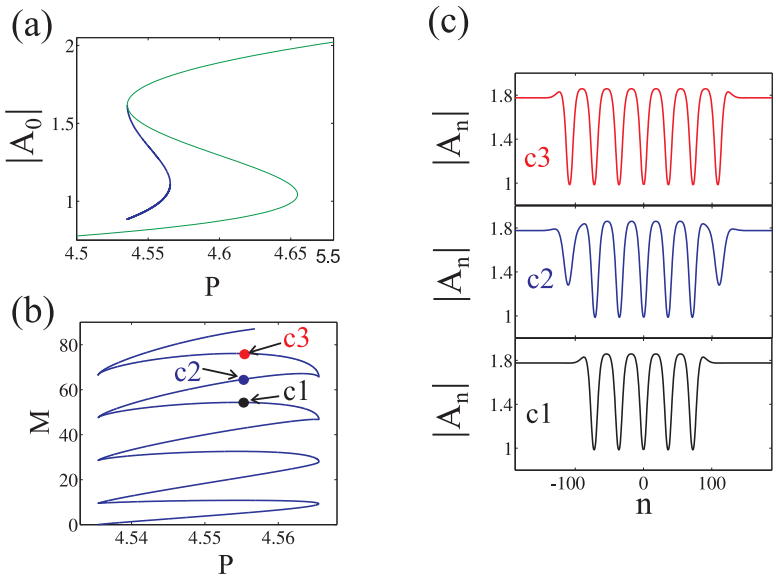

FIG. 4.7. *(a),(b) Similar to Fig. 4.4 but for* $\delta = 9.2 + 2i$. *(c) Field distributions of the solitons at the labelled points. The other parameters are* $\alpha = -10$ *and* $c = 15$.

5. Solitons for pure dissipative nonlinearity. For the final set of results, let us suppose that α is pure imaginary. We shall restrict attention to the case when $\mathrm{Re}(\delta) > 0$ and for simplicity shall focus on the continuum limit of large c. (We have also found bright and grey cavity solitons in the case of negative detuning $\mathrm{Re}(\delta) < 0$, which can also snake, but we found that the snakes never touch the boundary of the bistability region, and so there are no new bifurcation mechanisms other than those we have already described for other nonlinearities.)

For $\mathrm{Re}(\delta) > 0$, the upper and the lower homogeneous states can be stable, but in general have complex Floquet multipliers, so that small stationary perturbations decay to these states through oscillation. Bifurcation diagrams for bright and grey solitons are shown in Fig. 5.1 for the case of strong coupling $c = 15$. Within the windings of these thin snakes, stable portions are found of both the bright and grey soliton branches.

One can see that the rightmost fold point of the bifurcation diagram of bright

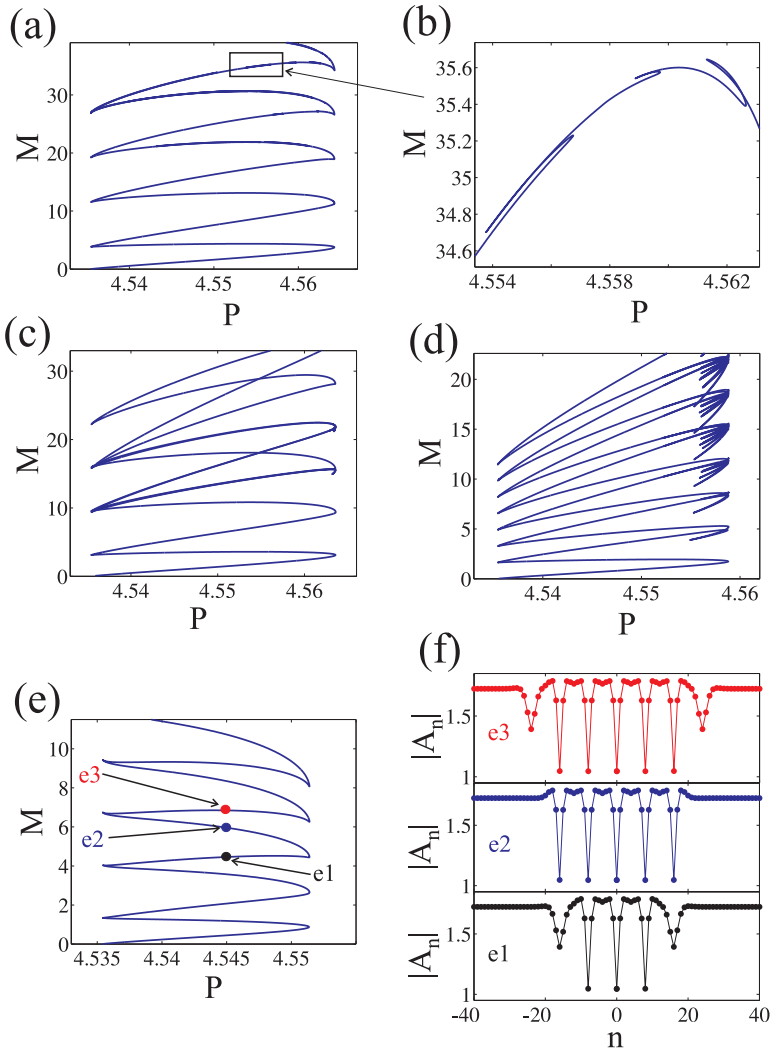

FIG. 4.8. *(a),(c),(d),(e) Similar to Fig. 4.7(b) but for (a) $c = 2.75$, (c) $c = 2$, (d) $c = 1$ and (e) $c = 0.5$. (b) A zoom that shows a detail of panel (a). (f) Solution profiles at the three labelled points in (e).*

solitons is quite close to the the right-hand edge of the bistability region. This point at $P = P_+$ corresponds to a fold of the homogeneous state in the tail of the bright soliton, so we can expect here a similar bifurcation sequence to occur as did for bright solitons with focusing nonlinearity (e.g. in Fig. 3.4). In the present case, the bifurcation leads to switching of the thin snaking curve from the fundamental soliton branch to a branch of multi-pulses, see Fig. 5.2. One can see that the field distributions in Fig. 5.2(c) that the closed solutions on the closed loops resemble orbits close to a Maxwell point between the lower homogeneous state and a large amplitude periodic state. Each of the left-hand (low P) folds in the bifurcation diagram corresponds to the increase of the soliton width by one period of the pattern state.

The bifurcation diagram for grey solitons can also split into separate branches, however, the point where this bifurcation happen is not related to a boundary of

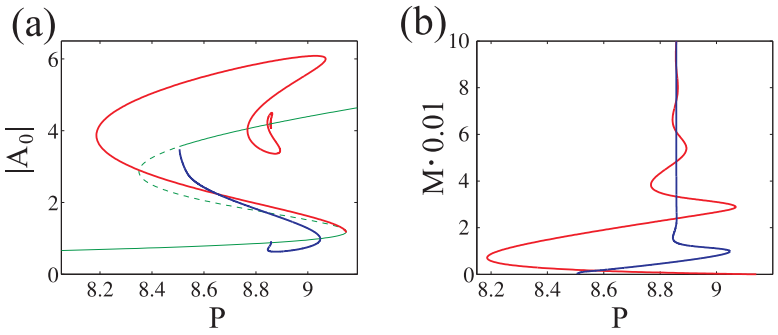

FIG. 5.1. *Similar to Fig. 4.3, but for parameters values* $\alpha = -16i$, $\delta = 1. + 17i$ *and* $c = 15$.

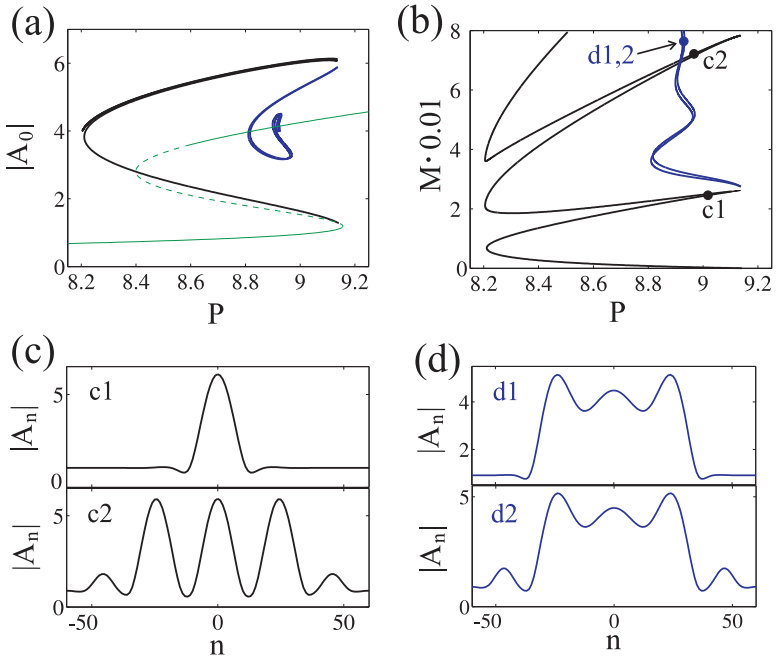

FIG. 5.2. *(a),(b) Similar to Fig. 5.1 but for the bright solitons only and* $\delta = 1.05 + 17i$. *Blue and black curves show disconnected portions of the bifurcation diagram of the bright solitons. (c), (d) Field distributions of the solitons at the labelled points. The other parameters are* $\alpha = -16i$ *and* $c = 15$.

the bistability region of the homogeneous state. In fact, grey solitons can exist also outside this region. At some point, the bifurcation curve for the grey soliton undergoes a transcritical bifurcation and intersects with a branch of multi-pulse solitons. This leads to the highly complex bifurcation diagram depicted in Fig. 5.3.

6. Conclusion. This paper has carried out a thorough examination of localised solutions (solitons) in a canonical spatially discrete model for a pumped optical lattice, both for the physically important case where losses are present, and in the mathematically simpler case where energy is conserved. We have also explored differences between the fundamentally discrete case (effectively $c \leq 1$) and approximations to the continuum limit (usually $c \geq 3$). Our main aim has been to elucidate the complex

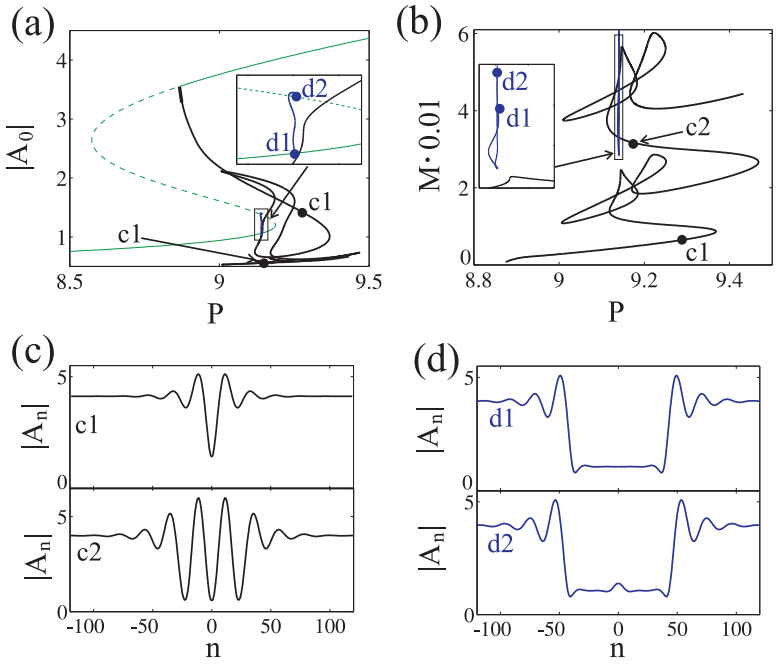

FIG. 5.3. *Similar to Fig. 5.2 but for grey solitons. The parameters are* $\alpha = -16i$, $\delta = 1.225{+}17i$ *and* $c = 15$.

topology of the branches of solitons in this context and to find mechanisms by which stable solitons can be created. We have seen a plethora of different snaking bifurcation diagrams inside different parameter regions where there is multiplicity between different spatially homogeneous states. By choosing a model with saturable nonlinearity, we have shown there to be several different parameter regions in which such bistability can occur. In particular we have found bistability for each of focusing, defocusing and pure dissipative nonlinearity. The novelty of this work is that we systematically study the effect of varying discreteness and dissipation on the formation of the solitons. We found that the mechanisms responsible for the soliton formation are very different in the near conservative and in the lossy cases and studied the chain of bifurcations the solitons undergo as the size of the loss term is varied.

A key outcome of this paper has been to identify various mechanisms by which snaking bifurcation diagrams of localised solutions can be created or destroyed as a second parameter varies:

- **Codimension-two local bifurcations**, for example sub- to super-critical transition for the spatial Hopf bifurcation at a modulation instability; or the death of the Maxwell point in a cusp bifurcation. An example of the former can be inferred from the two parameter diagram Fig. 3.6. Examples of the latter can be seen to the right of Fig. 3.6 and in Fig. 3.9(d) and (f).
- **Snake thinning** via passing to the continuum limit. For example, compare Figs. 3.3 and 3.8.
- **Snake death I: loop formation** by crashing into the fold of the tail homogeneous state of a soliton. For example, see Fig. 3.10.
- **Snake death II: isola formation** by crashing into the fold of the core homogeneous state that the soliton connects to at a Maxwell point. For

example, see Fig. 3.12

- **Snake explosions** caused by other changes of topology, involving interactions between Maxwell points caused by heteroclinic connections to homogeneous states and Maxwell points caused by heteroclinic connections to periodic states. See for example, Fig. 4.4 and Fig. 5.3 for evidence of more complex snaking diagrams caused by such transitions.

Future work will address mathematical unfoldings of some or all of these codimension-two mechanisms.

Proposition 2.1 has usefully shown a direct connection between stability of spatially homogeneous states and hyperbolicity of the corresponding fixed point of the equilibrium equations viewed as a iterated map in space. This latter condition is precisely what is required in order for there to be the possibility of persistent spatial localised solutions, which are homoclinic orbits of the map. Bistability between the upper and lower states then allows for persistent heteroclinic cycles (Maxwell points) between two distinct hyperbolic states. In general, it is the spatial discreteness in the model that opens up the pinning regions around Maxwell points that causes the existence of snaking bifurcation diagrams which in turn create new stable solitons. In fact, the snaking mechanism is responsible for opening up parameter regions (sometimes very wide) in which there is a multiplicity of distinct stable solitons states each of which have a distinct value of the mass M.

The results obtained in the paper suggest the possible technological importance of optical cavity arrays for formation and control of complicated localised structures in all-optical information processing. Another possible application could be the use of cavity solitons in semiconductor parametric oscillators. High-Q system with relatively low loss seem to be promising in this respect because they can operate at lower pump powers. At the same time, cavity solitons in systems with low loss have been investigated rather less then highly-dissipative cavity solitons. One of the reason for this is that only recently has there been a breakthrough in technology for high-Q optical micro-cavities needed to observe discrete cavity solitons with low losses [1, 29, 28]. In the present paper we address such solitons in the limit of small or zero loss, as well as explain how they relate to those cavity solitons that exist for high loss.

An important feature of the model considered here (1.1) is that it is spatially reversible. Since we can identify two reversibilities, then we have the possibility of two distinct classes of symmetric solutions, namely site-centred solitons and off-site centred. It is clear that there must also be spatially non-symmetric solutions, forming the 'ladders' that are known to connect the two opposing snakes [4, 2] in the context of spatially continuous systems. While such solutions are not necessarily stable as solutions of the initial-value problem, the study of non-symmetric solutions can be important for understanding the transition from resting to moving solitons. Indeed, the role of symmetries and the bifurcations responsible for the motion of the cavity solitons in the discrete case will be considered in subsequent work. There we will show how the bifurcation curve of the discrete solitons splits into isolas and how the isolas disappear when a sufficiently large gradient of the phase of the pump is introduced.

Acknowledgements. This work was funded by EPSRC Grant No. EP/D079225/1. The authors should like to thank Dimitry Skryabin for originally suggesting this work. Thanks also go to him and to Oleg Egorov, Andrey Gorbach and Gerard Iooss for helpful discussions.

REFERENCES

[1] D.K. Armani, T.J. Kippenberg, S.M. Spillane, and K.J. Vahala , *Ultra-high-Q toroid microcavity on a chip*, Nature (London), **421**, 925 (2003)
[2] M. Beck, J. Knobloch, D. Lloyd, B. Sandstede and T. Wagenknecht *Snakes, ladders and isolas of localized patterns*, To appear in SIAM J. Math. Anal. (2009)
[3] J. Burke, E. Knobloch, *Homoclinic snaking: structure and stability*, Chaos, **17**, Issue 3, 037102 (2007)
[4] J. Burke & E. Knobloch, *Localized states in the generalized Swift-Hohenberg equation*, Phys. Rev. E, **73**, 056211 (2006)
[5] A.V. Buryak, A.R. Champneys, *On the stability of solitary wave solutions of the fifth-order KdV equation*, Phys. Lett. A, **233**, issue 1-2, 58 (1997)
[6] A.R. Champneys, *Homoclinic orbits in reversible systems and their applications in mechanics, fluids and optics*, Physica D, **112**(1), p.158 (1998)
[7] A.R. Champneys, *Subsidiary homoclinic orbits to a saddle-focus for reversible systems*, Int. J. Bif. Chaos, **4**, 6, 1447 (1994)
[8] A.R. Champneys and J. Yang, *A scalar nonlinear bifurcation of solitary waves for coupled nonlinear Schrodinger systems*, Nonlinearity **15**, 2165 (2002)
[9] A. Champneys, J. Yang, B. Malomed and D. Kaup, *Embedded solitons: Solitary waves in resonance with the linear spectrum*, **152**, 340, (2001)
[10] S.-N. Chow C. Li and D. Wang *Normal Forms and Bifurcation of Planar Vector Fields* CUP, Cambridge (1994)
[11] P. Coullet , C. Riera and C. Tresser, *Stable static localized structures in one dimension* Phys. Rev. Lett. **84**, 3069 (2000)
[12] J.H.P. Dawes, *Localized pattern formation with a large scale mode: slanted snaking*, SIAM J. Appl. Dyn. Syst, **7**(1), 186, (2008)
[13] F. Dias and G. Iooss, *Capillary-gravity interfacial waves in infinite depth* Eur. J. MEC. B-FLUIDS **15**, 367 (1996)
[14] O.A. Egorov, U. Peschel, and F. Lederer, *Discrete quadratic cavity solitons*, Phys. Rev. E, **71**, 56612 (2005)
[15] O.A. Egorov and F. Lederer, Y.S. Kivshar, *How does and inclined holding beam affect discrete modulational instability and solitons in nonlinear cavities?*, Optics Express, **15**, 7, 4149 (2007)
[16] D. Gomilla and G.L. Oppo, *Subcritical patterns and dissipative solitons due to intracavity photonic crystals*, Phys. Rev. A, **76**, 043823 (2007)
[17] J. Haerterich, *Cascades of reversible homoclinic orbits to a saddle-focus equilibrium* Physica D, **112**, 187 (1996)
[18] G. Iooss and M.C. Perouème, *Perturbed homoclinic solutions in reversible 1:1 resonance vector fields*, J. Diff. Eqns, **102**, 62 (1993)
[19] J. Knobloch and T. Wagenknecht, *Homoclinic snaking near a heteroclinic cycle in reversible systems*, Physica D, **206**(1-2), 82 (2005)
[20] G. Kozyreff and S.J. Chapman, *Asymptotics of large bound states of localized structures*, Phys. Rev. Lett., **97**, 044502 (2006)
[21] B. Krasukopf, H.M. Osinga and J. Galan, *Numerical continuation methods for dynamical systems: path following and boundary problems*, Springer-Verlag (2007)
[22] J.S.W. Lamb and J.A.G. Roberts, *Time-reversal symmetry in dynamical systems: a survey*, Physica D **112**, 1 (1998)
[23] D.B. Lloyd, B. Sandstede, D. Avitabile and A.R. Champneys, *Localised patterns in the 2D Swift-Hohenberg equation*, to appear in SIAM J. Appl. Dyn. Syst. (2008)
[24] U. Peschel, O.A. Egorov, and F. Lederer, *Discrete cavity solitons*, Optics Letters, **29**, 1909 (2004)
[25] U. Peschel, D. Michaelis and C.O. Weiss, *Spatial solitons in optical cavities*, IEEE J. Quantum Electron. **39**, 51 (2003)
[26] Y. Pomeau *Front motion, metastability and subcritical bifurcations in hydrodynamics*, Physica D **23**(3), 111 (1986)
[27] L.P. Shil'nikov, A. Shil'nikov, D. Turaev and L. Chua, *Methods of qualitative theory in nonlinear dynamics, parts 1 and 2*, World Scientific Pub. Co., Inc., River Edge, NJ, (1998) and (2001)
[28] B.S. Song, S. Noda, T. Asano, and Y. Akahane , *Ultra-high-Q photonic double-heterostructure nanocavity*, Nature Materials, **4**, 207 (2005)
[29] K.J.Vahala , *Optical microcavities*, Nature (London), **421**, 925 (2003)
[30] P.D Woods and A.R. Champneys, *Heteroclinic tangles and homoclinic snaking in the unfolding of a degenerate reversible Hamilton-Hopf bifurcation*, Physica D, **129**(3), 130 (1999)
[31] A. Yariv,*Quantum Electronics*, Wiley, New-York (1989)

[32] A. Yulin, A.R. Champneys and D.V. Skryabin, *Discrete cavity solitons due to saturable nonlinearity*, Phys. Rev. A, **78**, 011804(R) (2008)